JGR Solid Earth

RESEARCH ARTICLE
10.1029/2019JB018560

Numerical Modeling of Mantle Flow Beneath Madagascar to Constrain Upper Mantle Rheology Beneath Continental Regions

T. A. Rajaonarison[1], D. S. Stamps[1], S. Fishwick[2], S. Brune[3,4], A. Glerum[3], and J. Hu[5]

[1]Department of Geosciences, Virginia Polytechnic Institute and State University, Blacksburg, VA, USA, [2]Department of Geology, University of Leicester, Leicester, UK, [3]GFZ German Research Center of Geosciences, Potsdam, Germany, [4]Institute of Earth and Environmental Sciences, University of Potsdam, Potsdam, Germany, [5]Division of Geological and Planetary Sciences, California Institute of Technology, Pasadena, CA, USA

Key Points:
- Asthenospheric flow patterns beneath Madagascar are predicted from edge-driven convection and mantle wind modeling
- Comparison of predicted shear wave splitting parameters with seismic anisotropy suggests a predominantly asthenospheric source
- Dislocation creep rheology extends into the asthenosphere beneath some continental regions

Supporting Information:
- Supporting Information S1

Correspondence to:
T. A. Rajaonarison,
trajaona@vt.edu

Citation:
Rajaonarison, T. A., Stamps, D. S., Fishwick, S., Brune, S., Glerum, A., & Hu, J. (2020). Numerical modeling of mantle flow beneath Madagascar to constrain upper mantle rheology beneath continental regions. *Journal of Geophysical Research: Solid Earth*, *125*, e2019JB018560. https://doi.org/10.1029/2019JB018560

Received 16 AUG 2019
Accepted 22 DEC 2019
Accepted article online 27 DEC 2019

Abstract Over the past few decades, azimuthal seismic anisotropy measurements have been widely used proxy to study past and present-day deformation of the lithosphere and to characterize convection in the mantle. Beneath continental regions, distinguishing between shallow and deep sources of anisotropy remains difficult due to poor depth constraints of measurements and a lack of regional-scale geodynamic modeling. Here, we constrain the sources of seismic anisotropy beneath Madagascar where a complex pattern cannot be explained by a single process such as absolute plate motion, global mantle flow, or geology. We test the hypotheses that either Edge-Driven Convection (EDC) or mantle flow derived from mantle wind interactions with lithospheric topography is the dominant source of anisotropy beneath Madagascar. We, therefore, simulate two sets of mantle convection models using regional-scale 3-D computational modeling. We then calculate Lattice Preferred Orientation that develops along pathlines of the mantle flow models and use them to calculate synthetic splitting parameters. Comparison of predicted with observed seismic anisotropy shows a good fit in northern and southern Madagascar for the EDC model, but the mantle wind case only fits well in northern Madagascar. This result suggests the dominant control of the measured anisotropy may be from EDC, but the role of localized fossil anisotropy in narrow shear zones cannot be ruled out in southern Madagascar. Our results suggest that the asthenosphere beneath northern and southern Madagascar is dominated by dislocation creep. Dislocation creep rheology may be dominant in the upper asthenosphere beneath other regions of continental lithosphere.

1. Introduction

The character of mantle convection with respect to flow patterns and rheological composition, particularly in the asthenosphere, remains open to debate varying from locally induced flow to models where global flow dominates (Moucha & Forte, 2011; Schuberth et al., 2009). Locally, one model for inducing small-scale convection in the asthenosphere can be driven by significant variations in lithospheric thickness known as edge-driven convection (EDC; i.e., King & Anderson, 1995, 1998). The model of EDC assumes a thermomechanical lithosphere such that the lithosphere-asthenospheric boundary is in thermal equilibrium. Variations in lithospheric thickness then induce thermal instabilities capable of driving asthenospheric flow. Characterizing EDC has been limited to 2-D modeling (e.g., Ballmer et al., 2015; Kaislaniemi & van Hunen, 2014) due to limitations in computational capabilities, yet newer finite element methods (Bangerth et al., 2018a, 2018b; Heister et al., 2017; Rose et al., 2017; Ramsay & Pysklywec, 2011) have made it possible to model 3-D regional mantle flow driven by lateral variations in lithospheric thickness.

Azimuthal seismic anisotropy is a commonly used proxy to characterize the patterns of convective motions of the Earth's interior (e.g., Long & Becker, 2010; Savage, 1999; Silver & Chan, 1991) although it cannot exclusively be associated with mantle flow. Some of the major contributors of seismic anisotropy may arise from (1) weaknesses in the crust (Nishizawa & Kanagawa, 2010), (2) melt lenses (Kendall, 1994), and/or fossil anisotropy (e.g., Silver & Chan, 1991) among other sources, and (3) the alignment of olivine minerals in the upper mantle governed by dislocation creep (Karato & Wu, 1993). Anisotropy in the crust can be from shallow sources due to the alignment of sheet silicates (e.g., Nishizawa & Kanagawa, 2010), faults, cracks, and microcracks in the upper 10–15 km (e.g., Kaneshima et al., 1988). Fossil anisotropy is crystallographic fabric

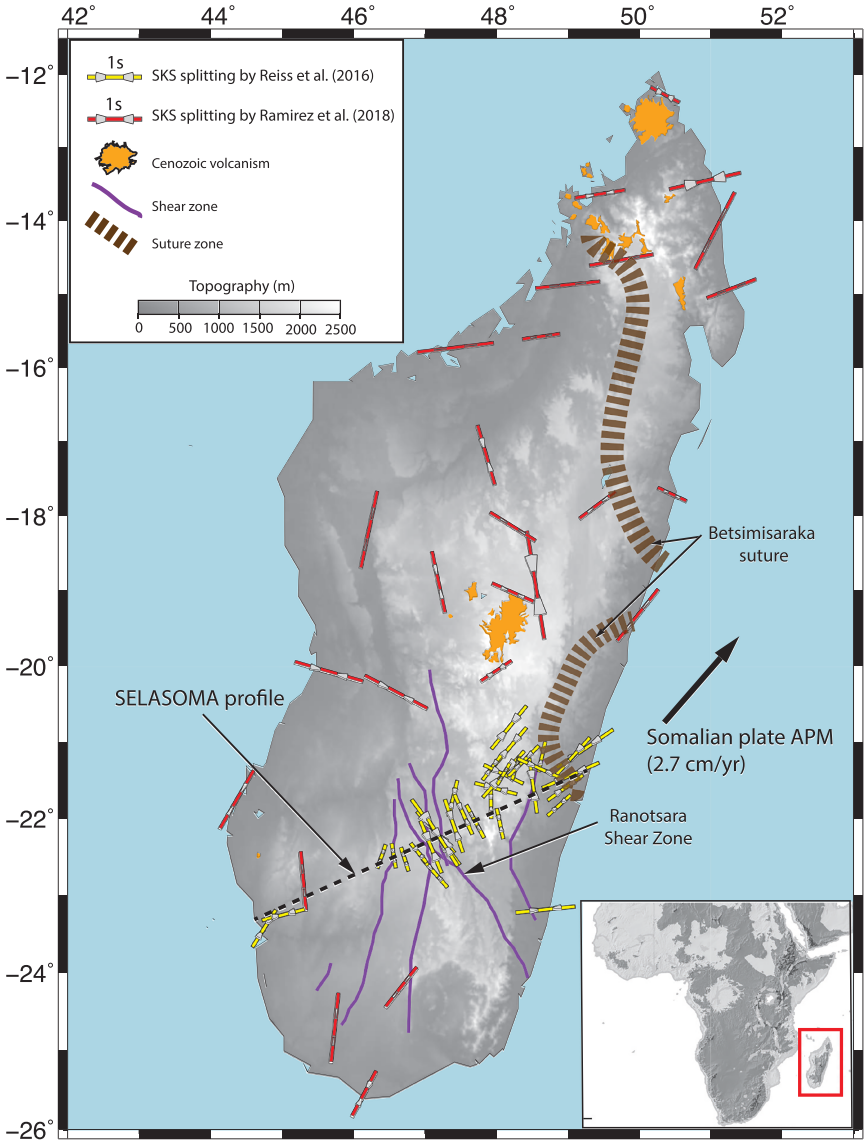

Figure 1. SKS splitting measurements across Madagascar. Red bars are splitting measurements from Ramirez et al. (2018). Yellow bars are splitting measurements (Reiss et al., 2016) from the SELASOMA profile (black dashed line). Gray wedges show confidence interval of the SKS splitting measurements. Orange regions represent Cenozoic volcanism. The black vector is the absolute plate motion direction (Argus et al., 2011). The background colors show topography.

preserved in the crust and/or lithospheric mantle imprinted by past or present-day orogenic processes (e.g., Tian & Santosh, 2015; Silver & Chan, 1988). In the upper mantle, mineral crystal aggregates (dominantly olivine) that are subject to dislocation creep align in the direction of mantle flow and the accumulated strain (Podolefsky et al., 2004). The resulting anisotropic fabrics are known as lattice preferred orientation (LPO) and are commonly mapped using a technique called SKS splitting.

Although the depth resolution of shear wave splitting measurements is poorly constrained, in nonvolcanic regions the potential sources reduce to preexisting weaknesses in the crust, fossil anisotropy, and mantle flow. In the simplified setting beneath oceanic lithosphere, seismic anisotropy may be caused by absolute plate motions (Beghein et al., 2014) or asthenospheric flow (Becker et al., 2014). However, limitations arise when interpreting seismic anisotropy in continental regions due to a lack of knowledge about subcontinental rheology and limited information on subcontinental mantle flow patterns.

Madagascar (Figure 1) is an ideal natural laboratory to study the sources of anisotropy beneath continental regions and the rheological implications for the lithosphere-asthenosphere system because (1) active volcanism is minimal or absent across most of the continental island, thus limiting the effect of melt lenses (Michon, 2016), (2) there are well-exposed tectonic fabrics for comparison (Collins & Windley, 2002; Schreurs et al., 2010), and (3) numerous geological and geophysical observations provide evidence of present-day tectonic activities potentially linked to viscous coupling to asthenospheric flow (Bertil & Regnoult, 1998; Kusky et al., 2010; Rambolamanana et al., 1997; Rindraharisaona et al., 2013).

Reiss et al. (2016) produced the first SKS splitting observations along the SELASOMA seismic profile (SEismological signatures in the Lithosphere/Asthenosphere System Of Southern Madagascar) that spans southern Madagascar in a NE-SW orientation, while Ramirez et al. (2018) provided additional SKS splitting measurements across the entire continental island (Figure 1). Azimuthal seismic anisotropy across Madagascar is quite complex. Along the SELASOMA profile, anisotropy varies from a NW-SE direction in the center of the profile to a SW-NE direction along its eastern and western sections (Figure 1, yellow bars). Reiss et al. (2016) interpret seismic anisotropy in the central part of the profile as sourced from the lithosphere in association with Precambrian ductile deformation at an existing narrow Ranotsara shear zone (see Figure 1) that strikes approximately NW-SE. In contrast, they attribute the SW-NE oriented observations to asthenospheric flow induced by absolute plate motion. Ramirez et al. (2018) suggest that asthenospheric upwelling related to the African superplume explains the homogeneous pattern of seismic anisotropy in northern Madagascar (Figure 1, red bars), but they suggest the complex pattern of anisotropy in central Madagascar is due to asthenospheric upwelling driven by delamination of the Malagasy lithosphere. Ramirez et al. (2018) also suggest that, since the observed anisotropy cannot be attributed to a single process such as absolute plate motion, the most likely source of the anisotropy is strain-induced LPO due to small-scale convective flow, which is poorly understood beneath Madagascar and surroundings.

In this work, we characterize EDC beneath Madagascar and investigate its contribution to the observed seismic anisotropy patterns to infer information about asthenospheric rheology. Previous studies suggest that interactions of mantle wind arising from global mantle flow with highly varying lithospheric thickness can explain small-scale variations of seismic anisotropy (e.g., Conrad & Behn, 2010). Therefore, in addition to the EDC model, we also test the interactions of mantle wind from two global mantle flow models (Behn et al., 2004; Forte et al., 2010) with the lithosphere beneath Madagascar. We use the finite element code Advanced Solver for Problems in Earth′s ConvecTion (ASPECT; Bangerth et al., 2018a, 2018b; Heister et al., 2017; Rose et al., 2017) to calculate 3-D EDC and mantle wind interactions with the lithosphere beneath Madagascar and surroundings using shear wave tomography-derived lithospheric thickness that incorporates all available seismic data of the region (updated Fishwick, 2010). Based on the modeled flow pattern, we use D-Rex (Kaminski & Ribe, 2001) to calculate LPO following the kinematic model for plastic deformation and dynamic recrystallization originally formulated by Ribe and Yu (1991) and further extended by Kaminski and Ribe (2001, 2002). Finally, we use calculated LPO as input to calculate synthetic splitting parameters (fast splitting direction and delay time) at the locations of seismic anisotropy observations using routines from FSTRACK (Becker et al., 2006), which we compare with observations. We find that the majority of seismic anisotropy observations can be explained with EDC and interactions with mantle wind from Behn et al. (2004), which suggests that dislocation creep extends into the upper asthenosphere beneath Madagascar.

This work yields new insights into present-day asthenospheric flow patterns beneath Madagascar. In addition, our work provides constraints on the dominant deformation mechanism of the upper asthenosphere. Our numerical experiments suggest that dislocation creep rheology may extend into the asthenosphere beneath continental regions and that accounting for dislocation creep flow laws is crucial for studies of sublithospheric mantle dynamics.

2. Tectonic History of Madagascar

Madagascar formed during the amalgamation of the Gondwana supercontinent 650 Ma (e.g., de Wit, 2003). The eastern part of Madagascar originated from the Indian Dharwar craton on eastern Gondwana and sutured with the western part of Madagascar, which was linked with the present-day African continent on western Gondwana. After the amalgamation of Gondwana via the subduction of the Mozambique Ocean, western Madagascar separated from the present-day Nubian Plate 160 Ma, and 50 Myr later, eastern Madagascar rifted from the Indian plate, resulting in the isolation of Madagascar, La Reunion, and the Comoros

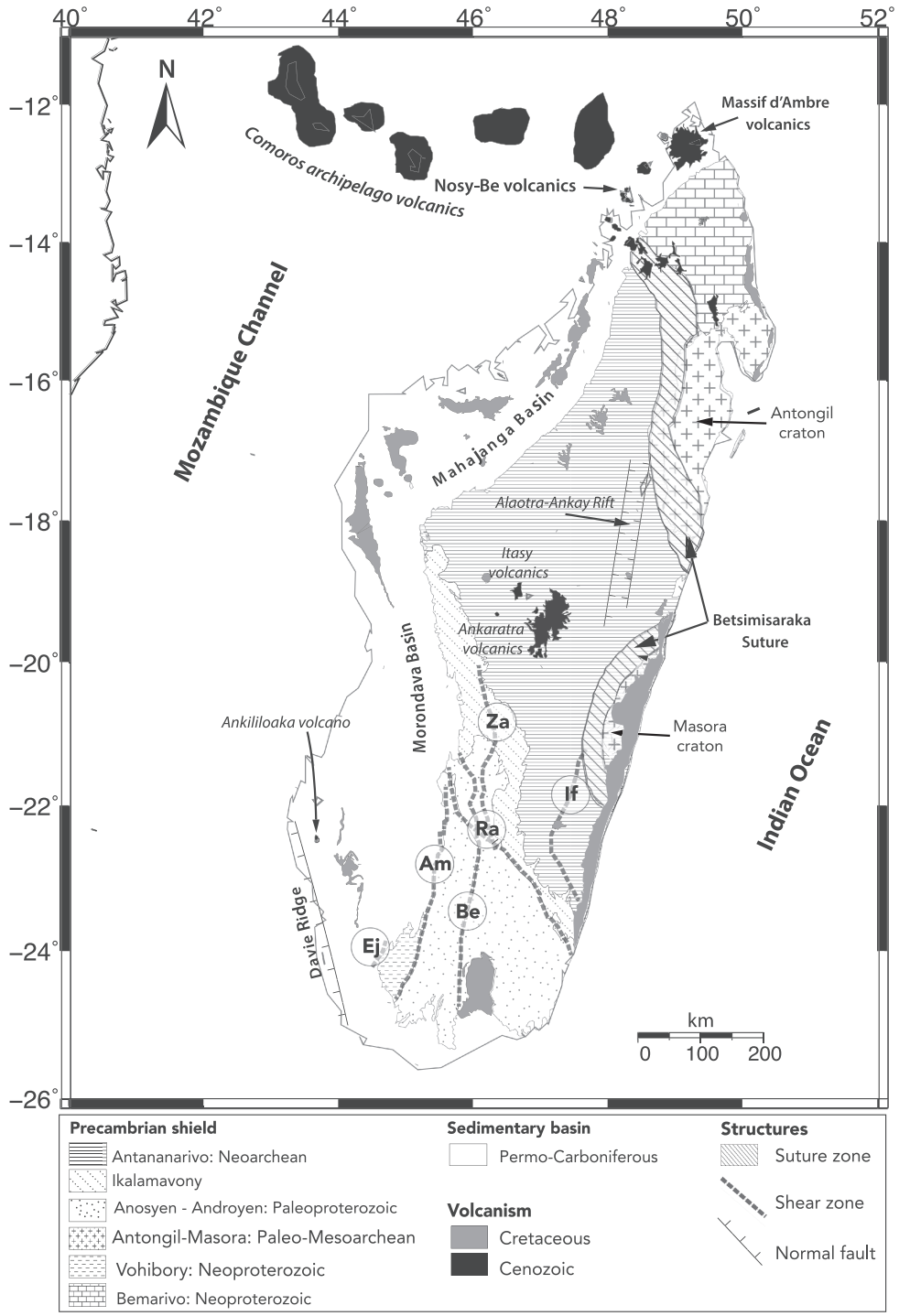

Figure 2. Simplified geologic map of Madagascar and the Comoros with key geologic features. Note the geological units (Tucker et al., 2012), Cretaceous (gray color) and Cenozoic (black regions) volcanism and major structures such as the Alaotra-Ankay Rift, Betsimisaraka suture zone (Collins & Windley, 2002), the Davies Ridge, and the shear zone in southern Madagascar. Dark gray dashed lines indicate shear zones from Martelat et al. (2000): Ej = Ejeda, Am = Ampanihy, Be = Beraketa, Ra = Ranotsara, If = Ifanadiana, Za = Zazafotsy.

islands. During these tectonic events, the Malagasy lithosphere was subjected to collisional and extensional events that shaped the present-day geological features in Madagascar, including a suture in central Madagascar, shear zones, and rifts (Figure 2). The geology of Madagascar is distinct from east to west, with Precambrian rocks in the eastern two thirds of the island and Paleozoic to recent sedimentary (Antsiranana, Morondava and Mahajanga basin) and Cretaceous volcanic rocks covering the west.

Eastern Madagascar is the location of an important Neoproterozoic suture zone, known as the Betsimisaraka suture. It separates Mesoarchean rock that is parallel to the east coast and the Precambrian Antananarivo block (West Gondwana; Collins, 2000; Collins & Windley, 2002; Collins et al., 2003). The Betsimisaraka suture is a highly deformed zone that consists of remnant consumed oceanic crust from the Mozambique Ocean which resulted from the collision between Eastern and Western Gondwana. Roughly trending N-S, the Betsimisaraka suture is divided into two segments, the northeastern segment that separates the Archean Antongil block and the Precambrian Antananarivo block (Raharimahefa & Kusky, 2009) and the southern segment that separates the Archean Masora block and the Precambrian Antananarivo block (Raharimahefa & Kusky, 2006; see Figure 2).

Southern Madagascar is a site of preexisting weaknesses, of which the most prominent are the Neoproterozoic Ampanihy, Vorokafotra, and the late Proterozoic/early Cambrian Ranotsara shear zones (Figure 2). These shear zones are thought to be composed of high-grade metamorphic rock and are associated with the orogenic evolution of the Mozambique (590–500 Ma) belt during the East African orogeny (Martelat et al., 2000). The N-S striking Apanihy and Vorkafotra shear zones are >450 km in length and between 10 and 20 km in width. The Ranotsara shear zone (Ra in Figure 2) differs from the other shear zones in that it is striking approximately NW-SE instead of N-S. Because of this oblique strike, it has been correlated with various shear zones in east Africa and southern India (Windley et al., 1994) and used to infer the paleoposition of India and Madagascar before the Gondwana breakup (de Wit et al., 2001; Nicollet, 1990). It crosscuts >400 km of the Malagasy Precambrian basement. Although the Ranotsara shear zone is typically considered as an intracrustal mega strike-slip shear zone with a sinistral sense of shear (e.g., de Wit et al., 2001), Schreurs et al. (2010) argue that the Ranotsara shear zone is a composite structure with ductile deflection in the central zone based on remote sensing and geologic observations. When Madagascar attained its current position with respect to Africa in the middle Miocene, lithospheric scale E-W extension began with the reactivation of N-S striking faults (Bertil & Regnoult, 1998) that formed rift basins such as the Alaotra-Ankay Rift (Figure 2). The late Proterozoic/early Cambrian Ranotsara Shear Zone has been reactivated with brittle faulting causing the formation of along-strike basins filled with Neogene sediments (de Wit, 2003; Schreurs et al., 2010).

Madagascar has undergone Cretaceous and minor Cenozoic intraplate magmatism and active volcanism. The eastern and coastal margins of Madagascar experienced voluminous basic lava extrusions that lasted at most 8 Myr during the late Cretaceous (Seward et al., 2004). The Cretaceous volcanics are sourced from the Marion hot spot, of which the volcano-tectonic interactions were responsible for magmatic rifting, thus allowing the breakup of India-Seychelles and Madagascar. The small Neogene-Quaternary volcanic regions are located in disparate locations along the island: at the northernmost tip of the island; along the Nosy-Be-Antongil axis (Massif d'Ambre and Nosy-Be Island); in the center (Itasy and Ankaratra volcanoes); and in the southwest (Ankililoaka volcanics; Figure 2).

3. Methods

3.1. Regional Scale 3-D Edge-Driven Convection Modeling

We simulate instantaneous regional mantle flow in a 3-D domain using the open source finite element code ASPECT v2.1.0 (Advanced Solver for Problems in the Earth's ConvecTion, Bangerth et al., 2018a, 2018b; Heister et al., 2017; Rose et al., 2017). This research software has been successfully applied to a wide range of geodynamic settings such as mantle convection (Austermann et al., 2017; Zhang & O'Neill, 2016), plume dynamics (Bredow, 2017; Dannberg & Gassmöller, 2018; Steinberger et al., 2019), continental rifting (Corti et al., 2019; Heron et al., 2018), and subduction (Glerum et al., 2018; Fraters et al., 2019). Using ASPECT, we solve for velocity, pressure, and temperature of the Stokes equations with the Boussinesq approximation, which consists of the equations of momentum, conservation of mass, and energy for incompressible fluid flow:

$$-\nabla \cdot [2\eta\varepsilon(\mathbf{u})] + \nabla p' = -\rho_0 \alpha T \mathbf{g} \qquad \text{in } \Omega, \tag{1}$$

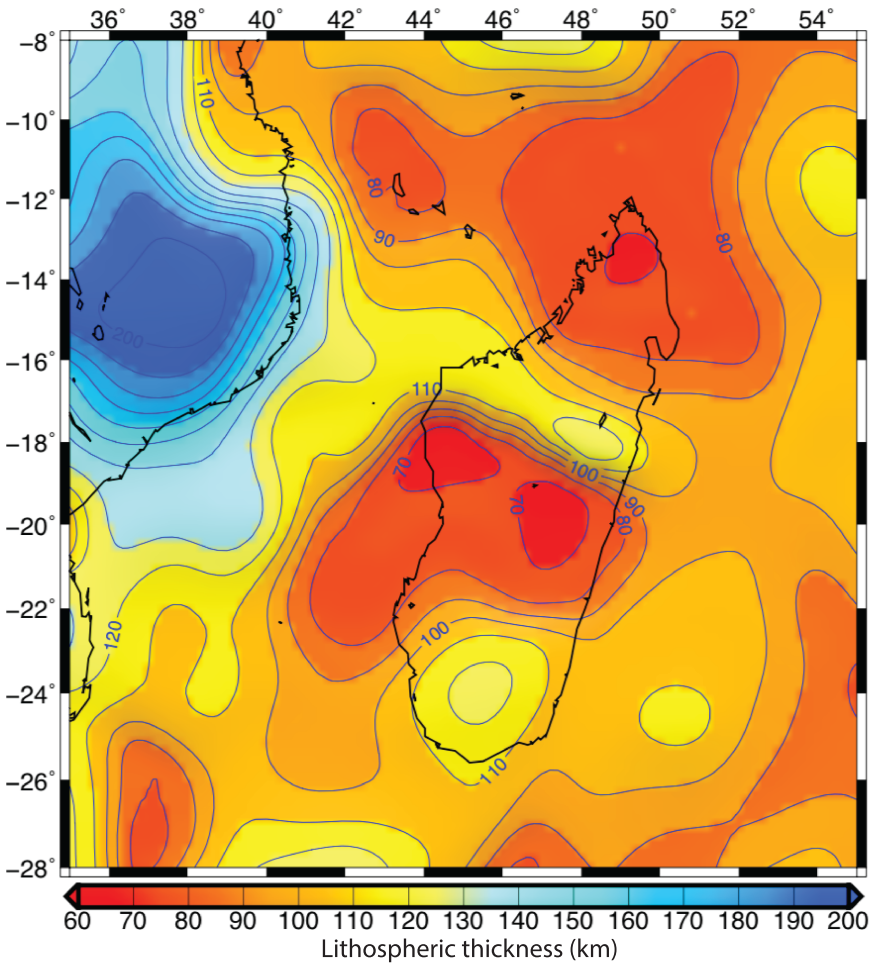

Figure 3. Lithospheric thickness model of Madagascar and its surroundings, updated from Fishwick (2010), which we use as an input for our study. Contours show lines of equal lithospheric thickness at 10 km intervals.

$$\nabla \cdot \mathbf{u} = 0 \qquad \text{in } \Omega, \tag{2}$$

$$\rho_0 C_p \left(\frac{\partial T}{\partial t} + \mathbf{u} \cdot \nabla T \right) - \nabla \cdot k \nabla T = \rho H \quad \text{in } \Omega. \tag{3}$$

$\varepsilon(\mathbf{u})$ is the symmetric gradient of velocity, η is viscosity, ρ is density, ρ_0 is the constant reference density, p' is dynamic pressure, T is temperature, $\mathbf{g}$ is gravitational acceleration, α is thermal expansion coefficient, κ is thermal conductivity, H is intrinsic specific heat production, and C_p is specific heat capacity. The effects of shear heating and adiabatic heating are neglected in the model. We employ the "single Advection, iterated Stokes" solver scheme, which solves the temperature and composition equation once at the beginning of each time step and then iterates out the solution of the Stokes equation. Our model domain is ~2,200 × 2,200 × 660 km along longitude, latitude, and depth, respectively, for a spherical chunk geometry. The model domain is initially globally refined and each element is ~34 × 34 × 10 km. The computation consists of 14 million unknowns solved on 192 cores. The model includes both lithosphere and sublithospheric mantle. The depth extent of 660 km is chosen as it corresponds to the 660 km seismic discontinuity associated with large viscosity increases (e.g., Forte & Mitrovica, 1996) and endothermic phase changes of olivine (Dziewonski & Anderson, 1981). Because of the phase change and the viscosity jump, we assume that the 660 km seismic discontinuity is an appropriate depth to investigate upper mantle flow.

The initial temperature field (Figures 4a and 5a) incorporates an approximate conductive and an adiabatic geothermal gradient. The initial thermal structure of the lithosphere is assumed to be a linear gradient from the surface (273 K) to the lithosphere-asthenosphere boundary. The base of the lithosphere is a thermomechanical boundary where the temperature is 1673 K, which is generally the upper bound of the

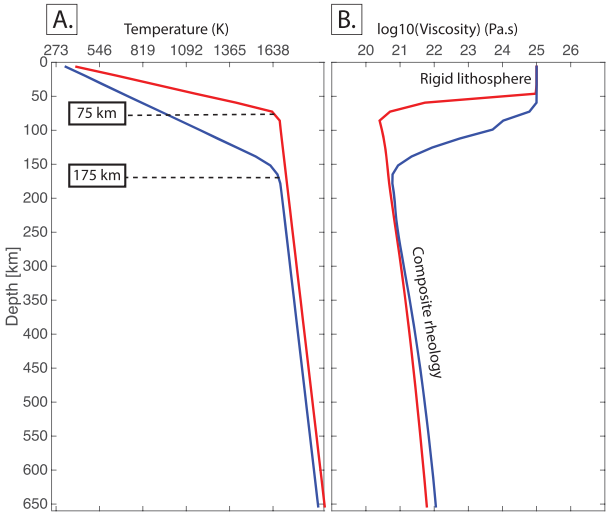

Figure 4. (a) One-dimensional temperature depth profiles for a lithospheric thickness of 75 km (red) and 175 km (blue). The temperature at the base of the lithosphere (1673 K) corresponds to the intersection of the conductive and adiabatic geothermal gradients. (b) Corresponding viscosity profiles for 75 km (red) and 175 km (blue) thick lithosphere.

mantle potential temperature (Hirschmann, 2010; Langmuir et al., 1992; Stixrude & Lithgow-Bertelloni, 2007). We choose the 1673 K because it is the estimated geophysical average of global mantle potential temperature according to Anderson (2000). The sublithospheric mantle temperature increases approximately adiabatically (0.5 K/km) to the base of the model.

The updated lithospheric structure model of Fishwick (2010) is mapped into the 3-D domain for Madagascar and surroundings (Figure 3). The lithospheric thickness is thinnest in central (~70–80 km) and northern (~70–80 km) Madagascar with a NW-SE trending belt of thicker lithosphere between the two regions (~110–120 km). In southern Madagascar the lithosphere is thicker compared to central Madagascar (~110–120 km). The lithospheric structure produces lateral variations in temperature such that relatively thick lithosphere features smaller geothermal gradients and is relatively cooler than thinner lithosphere (Figure 4a).

The lithosphere is assumed to be in a thermal steady state and without internal deformation, which is implemented by imposing a strong uniform viscosity of 10^{25} Pa s (Figures 4b and 5b). We assume that the composition of the underlying mantle is dry olivine and that the viscosity is governed by composite rheology (Jadamec & Billen, 2010). Composite rheology is a harmonic average of viscosity from diffusion creep (η_{diff}) and dislocation creep (η_{disl}) mechanism of olivine. The composite viscosity η_{comp} is given by

$$\eta_{\text{diff,disl}} = \frac{1}{2} A^{-\frac{1}{n}} d^{\frac{m}{n}} \dot{\epsilon}^{\frac{1-n}{n}} \exp\left(\frac{E_a + V_a P}{nRT}\right) \tag{4}$$

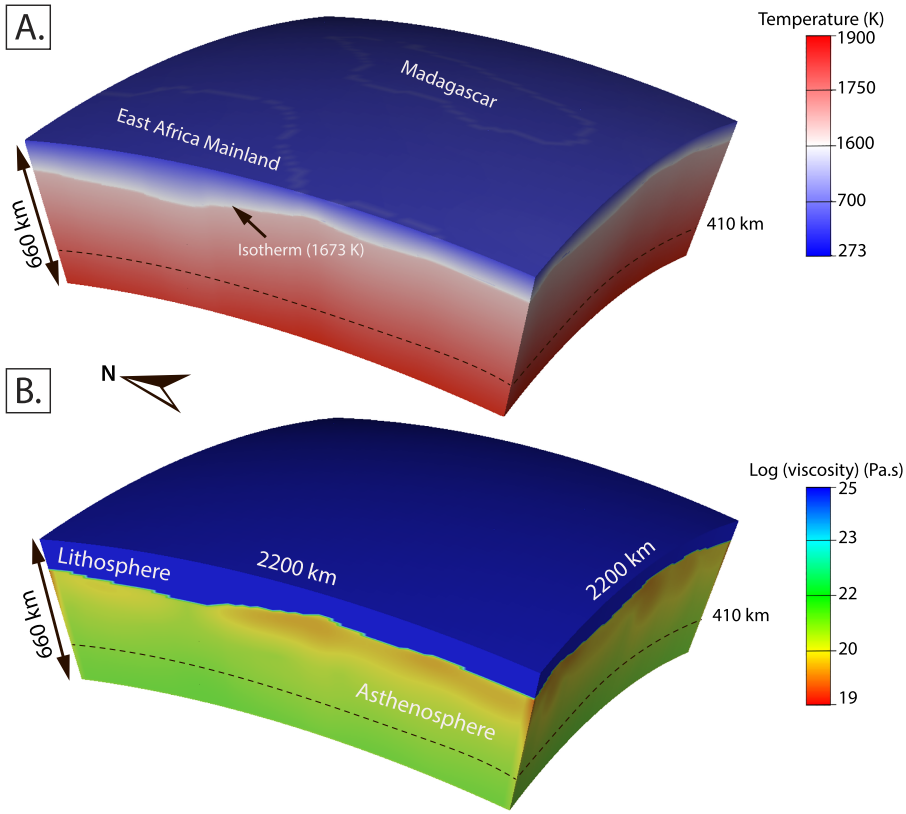

Figure 5. Numerical model setup: (a) Initial temperature condition. (b) Initial viscosity field.

Table 1
Parameters Used for EDC Simulation

Parameter	Symbol	Value	Unit
Reference density	ρ_0	3,300	kg/m^3
Thermal conductivity	κ	3	W·m^{-1}·K^{-1}
Specific heat capacity	C_p	1.25×10^3	J·kg^{-1}·K^{-1}
Intrinsic specific heat production	H	7.4×10^{-12}	W/kg
Thermal expansion coefficient	α	4×10^{-5}	K^{-1}
Gravitational acceleration	g	PREM	m/s^2

$$\eta_{\text{comp}} = \frac{\eta_{\text{diff}}\eta_{\text{disl}}}{\eta_{\text{diff}} + \eta_{\text{disl}}} \tag{5}$$

$\dot{\epsilon}$ is the square root of the second invariant of the strain rate tensor, T is temperature, P is pressure, E_a is activation energy, V_a is activation volume, n and m are, respectively, the stress and grain size exponents, A is preexponent factor, and R is the gas constant. The parameters A, E_a, V_a, n, and m are obtained from experimental studies of the olivine mineral from Hirth and Kohlstedt (2003) and their values are given in Table 2. The material of each layer (i.e., lithosphere and sublithospheric mantle) is tracked through compositional fields, which carry properties of the Earth's material within the convective flow. Using compositional fields allows for smoothing across compositional boundaries, which is needed to solve for sharp variations in the viscosity model, which are also smoothed.

The viscosity at each quadrature point is calculated using a harmonic average of the compositional fields weighted by the volume fraction of each composition at the same location (Figures 4b and 5b). The velocities at the sides and base of the model are set to zero and the surface is free-slip to neglect all effects of global mantle flow and to enhance regional resolution such that we can test our hypothesis regarding EDC. The velocities at the bottom boundary are set to zero to account for the high viscosity jump across the transition zone. The temperature boundary conditions at all boundaries are fixed so that net heat flux at the boundaries is zero.

3.2. Modeling Mantle Wind Interactions With the Lithosphere

To test lithosphere-mantle wind interactions based on the Behn et al. (2004) and the Forte et al. (2010) global mantle flow models, we subsequently impose velocity boundary conditions that align with global mantle flow at the vertical boundaries (west, north, south, and east) of our regional model and use the same initial conditions as the EDC model. We simulate two mantle wind models using horizontal mantle flow from (1) Forte et al. (2010) that is trending ~N20°E and (2) Behn et al. (2004), which is oriented ~N80°E. Both studies found a similar mantle flow velocity relative to Madagascar of ~10 mm/year, which is why we use this value in both scenarios. In order to simulate the mantle wind, our reference coordinate system is fixed to Madagascar, thus we impose a zero velocity boundary condition at the vertical boundaries in lithospheric regions. Given the highly varying lithospheric thickness at the vertical boundaries (Figure 3), the zero velocity boundary condition is imposed to regions shallower than the maximum lithospheric thickness of the model (≤200 km depth), while we impose mantle flow velocities below 200 km depth at all vertical boundaries. These velocity boundary conditions have the same magnitude and orientation at all vertical boundaries so that inflow and outflow are balanced as required by the incompressible model (equation (2)).

Table 2
Parameters Used for the Viscosity Flow Law of the Sublithospheric Mantle for Dry Olivine

Parameter	Symbol	Dislocation creep	Diffusion creep	Unit
Grain size	d	—	10×10^3	μm
Grain size exponent	m	—	3	—
Activation energy	E_a	530×10^3	375×10^3	J/mol
Activation volume	V_a	18×10^{-6}	6×10^{-6}	m^3/mol
Prefactor	A	6.52×10^{-16}	1.5×10^{-15}	-
Stress exponent	n	3.5	1.0	—

3.3. Estimating Shear Wave Splitting Parameters

In a first step, we use the program D-Rex (Kaminski et al., 2004) to predict sublithospheric LPO that develops beneath Madagascar as a result of EDC. We calculate synthetic LPO of olivine polycrystalline aggregates following the kinematic model for plastic deformation, grain boundary sliding, and dynamic recrystallization originally formulated by Ribe and Yu (1991) and further extended by Kaminski & Ribe (2001, 2002). All crystallographic input parameters are obtained from Kaminski et al. (2004) and from Becker et al. (2006), where the dimensionless parameters $\lambda^* = 5, M^* = 125$, and $\chi = 0.3$ are, respectively, the nucleation rate, the intrinsic grain boundary mobility, and the threshold volume fraction below which grain boundary sliding takes place.

Using D-Rex, we follow tracers to calculate accumulated synthetic LPO that develops along pathlines in the EDC flow field assuming steady state flow. A single tracer represents a mineral aggregate consisting of 2, 000 virtual grains of olivine (70%) and enstatite (30%) crystals (Kaminski et al., 2004), which represents a harzburgite composition. Since there is sensitivity of LPO with resolution, the flow field is interpolated onto a 15×15 km horizontal grid with 10 km depth resolution to capture variations in LPO patterns that may occur. Following the approach of Becker et al. (2006), the initially unstrained tracers are placed at starting positions at different depths below the locations where observations exist (Figure 1). We restrict the tracers to locate between a depth of 100 and 400 km with a vertical interval of 25 km to ensure asthenospheric material is captured beneath thinner lithosphere (Figure 3). The trajectory of each tracer is computed by advecting the tracer backward in time using the fourth-order Runge-Kunta advection scheme described in Becker et al. (2003). The backward advection is stopped when tracers either accumulate critical strain, a maximum advection time of 40 Ma is reached, or they arrive at a threshold depth of 410 km, below which mineral fabrics are erased at the transition zone.

The critical strain is a logarithmic saturation strain ξ_c, defined as the minimum of $\log(e_1/e_2)$ and $\log(e_1/e_3)$, where e_1, e_2, and e_3 are the largest, intermediate, and smallest eigenvalue of the finite strain ellipsoid, respectively. Ribe (1992) shows that ξ_c controls the strength of the anisotropy and a $\xi_c \geq 0.5$ is required to match the natural heterogeneity of LPO found in upper mantle xenoliths. Here, the fabrics are calculated up to a saturation $\xi_c = 0.75$ still following Becker et al. (2006). At the location where the tracer reaches ξ_c, it is set with randomly oriented crystals to form isotropic mantle and advected forward until it reaches the position from which it has been initially distributed. To minimize the diffusion creep contribution, we scale the strain rate tensor with the viscosity ratio $\gamma = \frac{\eta_{\text{diff}}}{\eta_{\text{disl}}}$ during the forward advection.

As the mineral aggregates accumulate finite strain, LPO develops and evolves along the pathlines in response to shear. D-Rex outputs the volume fractions and orientations of individual crystals that form the aggregates (collectively called the orientation distribution function). The orientation distribution function and single-crystal elastic tensors of olivine-enstatite provided by D-Rex are used to calculate the global elastic tensor of the grain assemblage using the Voigt averaging scheme. Considering the dominant hexagonal anisotropy of the elastic tensor, the orientation of the symmetric axis of the elastic tensor is calculated, which is known as the transverse isotropic approximation (TI). TI indicates the direction of elastic anisotropy that has been a widely used proxy for LPO (e.g., Becker et al., 2006; Faccenda & Capitanio, 2012; Hu et al., 2017).

In a second step, we use the elastic tensors of the olivine-enstatite aggregates calculated in step one as input for FSTRACK (Becker et al., 2006). FSTRACK calculates synthetic splitting parameters (fast direction Φ and delay time δt) where measurements exist (Figure 1). Synthetic seismograms are computed for an Earth model of multilayer anisotropy using the cross-correlation method developed by Menke and Levin (2003). The program constructs a stack of horizontal layers that are 25 km thick and centered at 100 to 400 km with a 25 km interval and defined by the elastic tensors of the olivine-enstatite aggregates below the seismic stations. Then FSTRACK computes the synthetic seismograms by calculating the sum of the harmonic responses of rays (over a range of frequencies >0–25 Hz) vertically polarized at a 5° incident angle, traversing the horizontal layers. The resulting seismograms are filtered by a band-pass filter with frequency cutoffs from 0.1–0.3 Hz that represent the typical frequency band for SKS waves (e.g., Faccenda & Capitanio, 2012, 2013). Due to dependence of splitting parameters on back azimuth (Becker et al., 2006), a set of fast polarization directions and delay times are calculated with elastic tensors rotated about the vertical axis around 360° with an increment of 2°. The circular mean of the fast directions and mean delay times represent the synthetic splitting at each station.

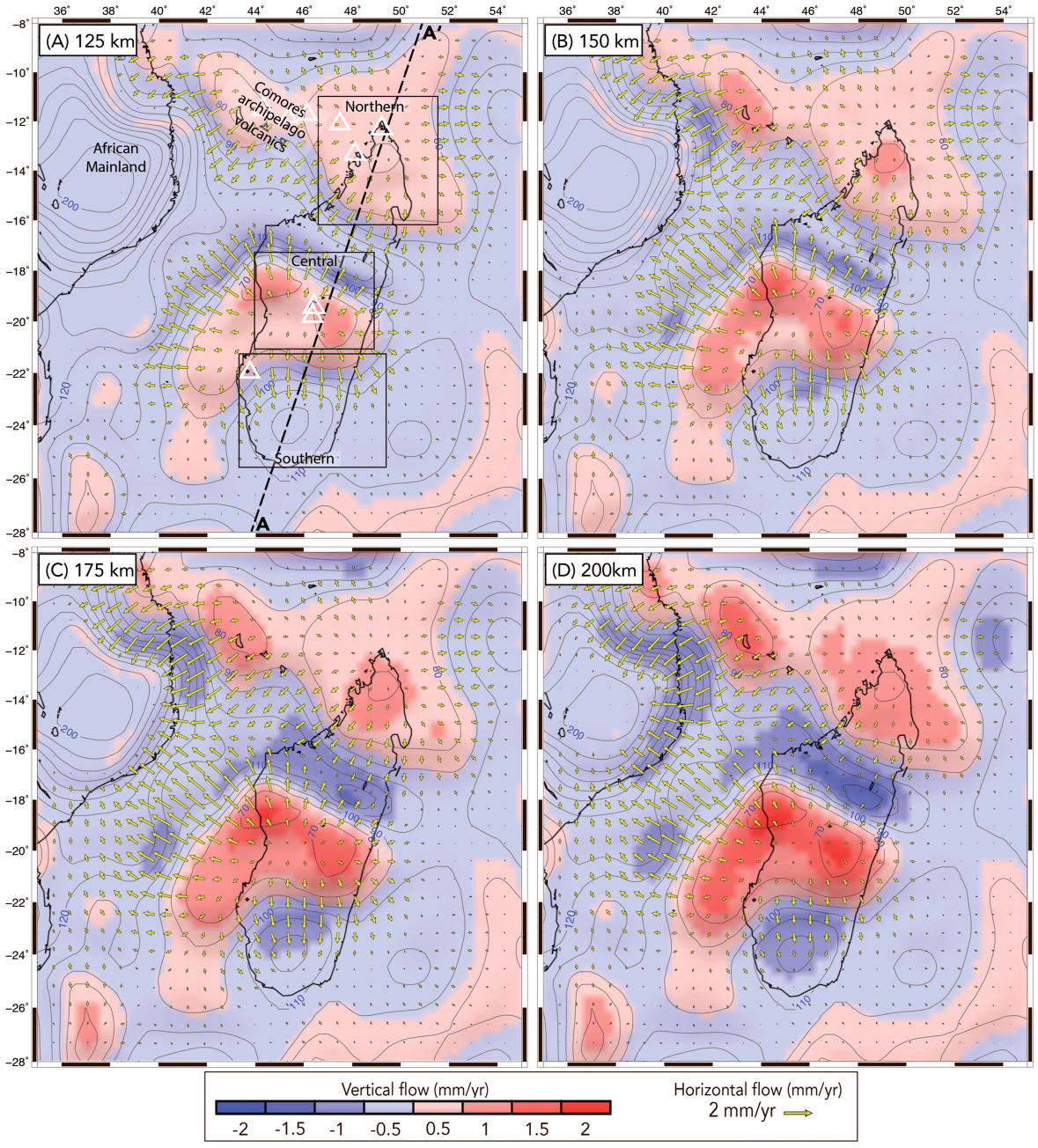

Figure 6. Depth slices showing EDC beneath Madagascar at (a) 125, (b) 150, (c) 175, and (d) 200 km depths at initial time (Time = 0 Ma). Background color indicates vertical flow. Yellow vectors portray horizontal flow. We infer two regions below Madagascar that are dominated by upwelling and two regions with downwelling. White triangles in (a) indicate Cenozoic volcanic regions which are also illustrated in Figure 2.

4. Results

4.1. Edge-Driven Convection Beneath Madagascar

Results of the 3-D simulations show that EDC forms where the lithosphere transitions from thin to thick (see Figure 3). Figure 6 portrays map views of the EDC flow field beneath Madagascar and surroundings at different depth slices with the background colors showing vertical motions and the vectors indicating horizontal motions at that depth. Cold downward flow occurs beneath thick lithosphere and upwelling occurs beneath relatively thin lithosphere. Hence, upwelling and diverging asthenospheric flow is located beneath central and northern Madagascar (Figure 6a) as well as beneath the Comoros archipelago volcanics in regions where the lithosphere is relatively thin.

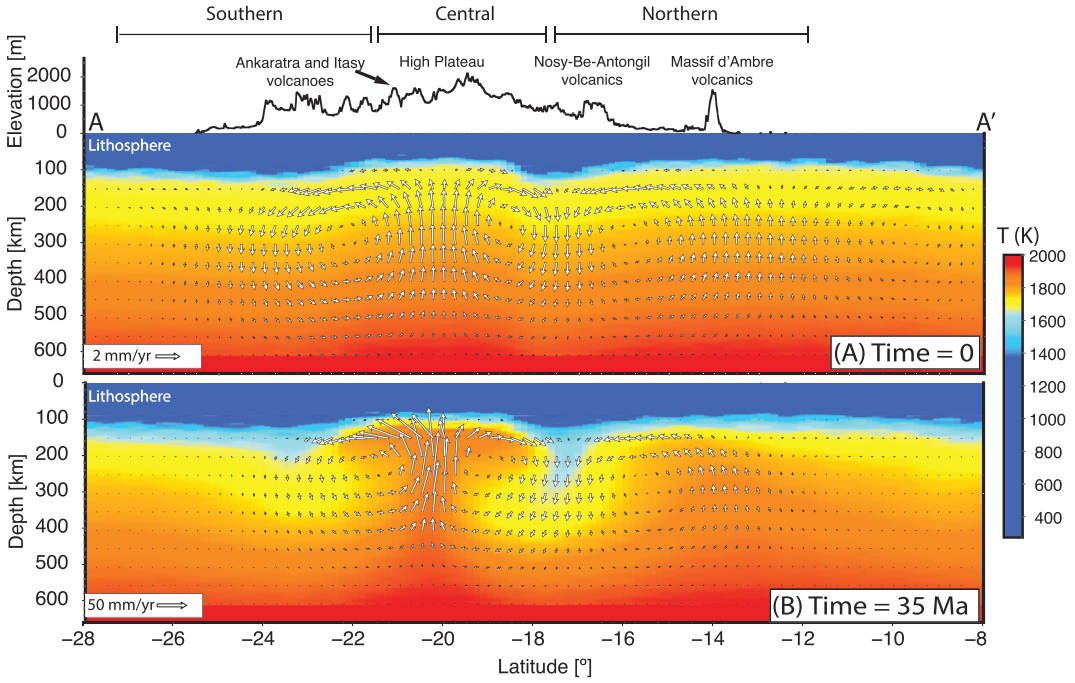

Figure 7. Profile showing time-dependent convection across the long axis of Madagascar (profile AA' in Figure 6). (a) Time = 0 Ma. (b) Time = 35 Ma. Note the similarity in the structures of mantle flow beneath the continental island.

In northernmost Madagascar, a region of relatively thin lithosphere (~70–80 km) lies adjacent to a belt of ~120 km thick lithosphere that strikes NW-SE and gradually increases in thickness toward the African mainland. As a result, this region develops asthenospheric upwelling in northern Madagascar (~0.5 mm/yr vertical velocity) and downwelling beneath the belt of thick lithosphere (~1 mm/yr vertical velocity; Figure 6). The corresponding horizontal velocity shows a radial outward flow asymmetrically spreading to the ENE direction at the eastern side of the northern region and to the SW direction at the western side of the northern region that ranges from ~0.1–1 mm/yr (Figures 6a–6d). Beneath the Comoros archipelago volcanics, upwelling increases to ~2 mm/yr at 200 km depth, due to the sharp increase in lithospheric thickness variation beneath the African mainland.

Central Madagascar features the largest zone of thin lithosphere (~60–70 km) across the continental island. It is bounded to the north by the belt of thick lithosphere that strikes approximately NW-SE, to the south by thick lithosphere (~120 km), and further to the west by the thickest lithosphere (~200 km) within the African mainland. The lithospheric thickness configuration induces a relatively stronger and broad upwelling beneath central Madagascar from 250–125 km depths, which has been hypothesized by Reiss et al. (2016). The horizontal velocity shows a radial pattern with the minimum horizontal velocity at the center of Madagascar where the flow is mostly vertical. The strength of upwelling in central Madagascar increases with depth.

Asthenospheric flow beneath southern Madagascar is characterized by pronounced downwelling as shown in Figure 6. There is a minor shift in orientation of horizontal flow between shallower and deeper regions. At 125 and 150 km depths, the flow pattern in the transition between central and southern Madagascar features a southward direction of horizontal flow. Vertical downwelling is also more prominent at shallower depths in the center of southern Madagascar shown by the low-magnitude horizontal vectors.

In order to assess the temporal stability of EDC beneath Madagascar and the robustness of our results, we simulate the flow field up to a maximum time of 35 Ma. Figures 7a and 7b show EDC and temperature along the long axis of Madagascar, profile AA' defined in Figure 6a at $t = 0$ and at $t = 35$ Ma, respectively. The velocity and temperature fields along the profiles illustrate how EDC is initiated from the lateral variations in temperature and the associated buoyancy forces. There are three pronounced steps in lithospheric thickness across the long axis of Madagascar, which, in turn, generate three convection cells centered at 22°S, 18°S, and 16°S that spread to the base of the model domain. Longer wavelength variations in lithosphere thickness

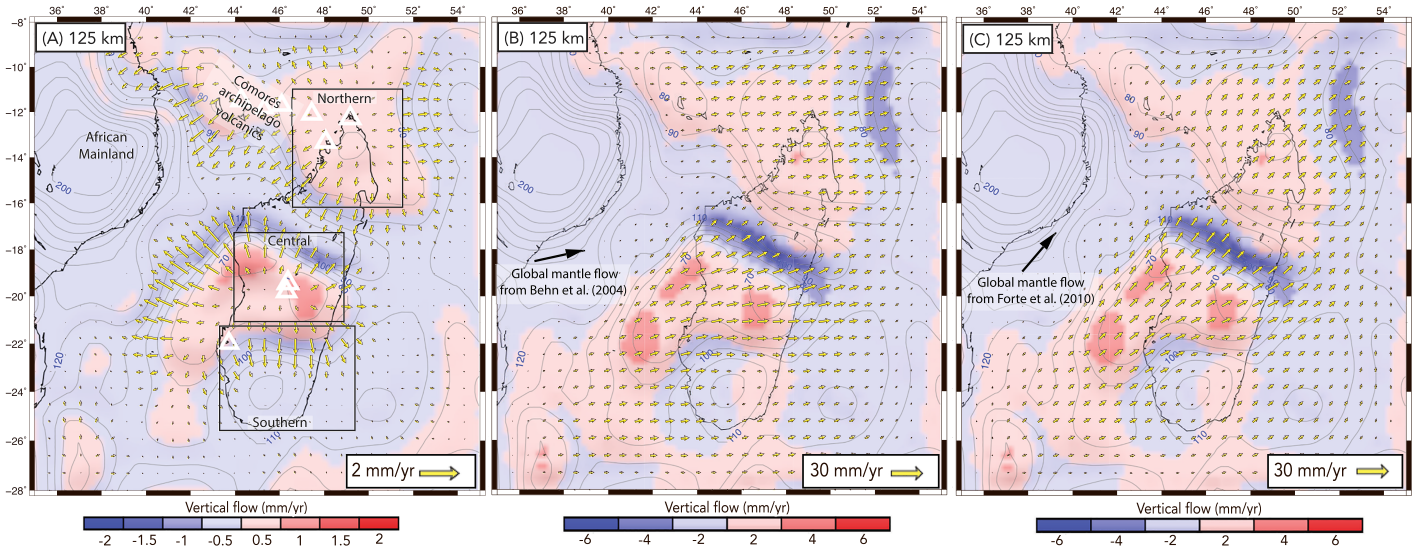

Figure 8. Depth slices showing mantle flow fields at initial time (Time = 0 Ma) at 125 km. (a) for EDC model, (b) from mantle wind of Behn et al. (2004) global mantle flow, (c) from mantle wind of Forte et al. (2010) global mantle flow. Background color indicates vertical flow. Yellow vectors portray horizontal flow. The vertical flow show similar pattern for all models where we infer two regions below Madagascar that are dominated by upwelling and two regions with downwelling. White triangles in (a) indicate Cenozoic volcanic regions which are also illustrated in Figure 2. Black arrows in (b) and (c) indicate the direction of mantle wind of Behn et al. (2004) and Forte and Mitrovica (1996), respectively.

induce wider convection cells as seen beneath northernmost Madagascar, while steeper variations generate smaller convection cells, such as in central Madagascar.

At both $t = 0$ and $t = 35$ Ma, central Madagascar is the site of diverging upwelling and adjacent downwelling that occurs beneath southern Madagascar and the belt of thicker lithosphere to the north. At the initial stage ($t = 0$), downwelling and upwelling asthenospheric flows located in and around central Madagascar have similar magnitudes with a maximum velocity of 2 mm/yr, whereas upwelling is generally faster (~50 mm/yr) and more focused in central Madagascar at t =35 Ma because hotter mantle materials are brought to shallower depths. The velocity magnitude of 2 mm/yr from EDC at $t = 0$ is consistent with the expected weak flow of EDC (e.g., King & Anderson, 1998), whereas the ~50 mm/yr velocity magnitude at $t = 35$ Ma is in the range of large-scale mantle flow (e.g., Moucha & Forte, 2011; Schuberth et al., 2009). In northern Madagascar there is a broad region of upwelling that is similar in magnitude and direction over the 35 Ma time frame. The main result of this comparison is that the main asthenospheric structures are stable over geological time frames.

As an additional robustness test, we assess the behavior of our model with respect to uncertainties associated with lithospheric thickness derived from shear wave tomography. We address this point by conducting simulations where we vary the lithospheric thickness between +10 and −10 km. In all cases we find that the structure of the convective flow remains stable through time with upwelling beneath central and northern Madagascar and adjacent downwelling.

4.2. Mantle Wind Interactions With Lithosphere Beneath Madagascar

Figures 8a–8c show asthenospheric flow at 125 km all three models (EDC, Behn et al., 2004, and Forte et al., 2010, respectively). Horizontal velocities of the Behn et al. (2004) model (Figure 8b) shows mostly ~N80°E trends with magnitudes of 20–30 mm/yr across Madagascar and surroundings. These horizontal velocities are not significantly deflected at the transition from relatively thick to thin lithosphere. However, the magnitude of the horizontal velocities is 3 times that of the mantle wind applied at the boundaries. This increase in velocity magnitude beneath Madagascar is in response to the low-viscosity channel in sublithospheric regions. The vertical velocity shows a similar pattern as the EDC, that is, localized upwelling beneath northern and central Madagascar (~4 mm/yr vertical velocity), downwelling beneath the belt of thick lithosphere (~6 mm/yr vertical velocity), and downwelling beneath southern Madagascar (~2 mm/yr vertical velocity).

Figure 8c shows the mantle flow results from mantle wind model of Forte et al. (2010). Horizontal velocities show a mostly ~N20°E trend with magnitudes of 20–30 mm/yr across Madagascar and surroundings. The vertical velocities also show a pattern similar to the EDC models.

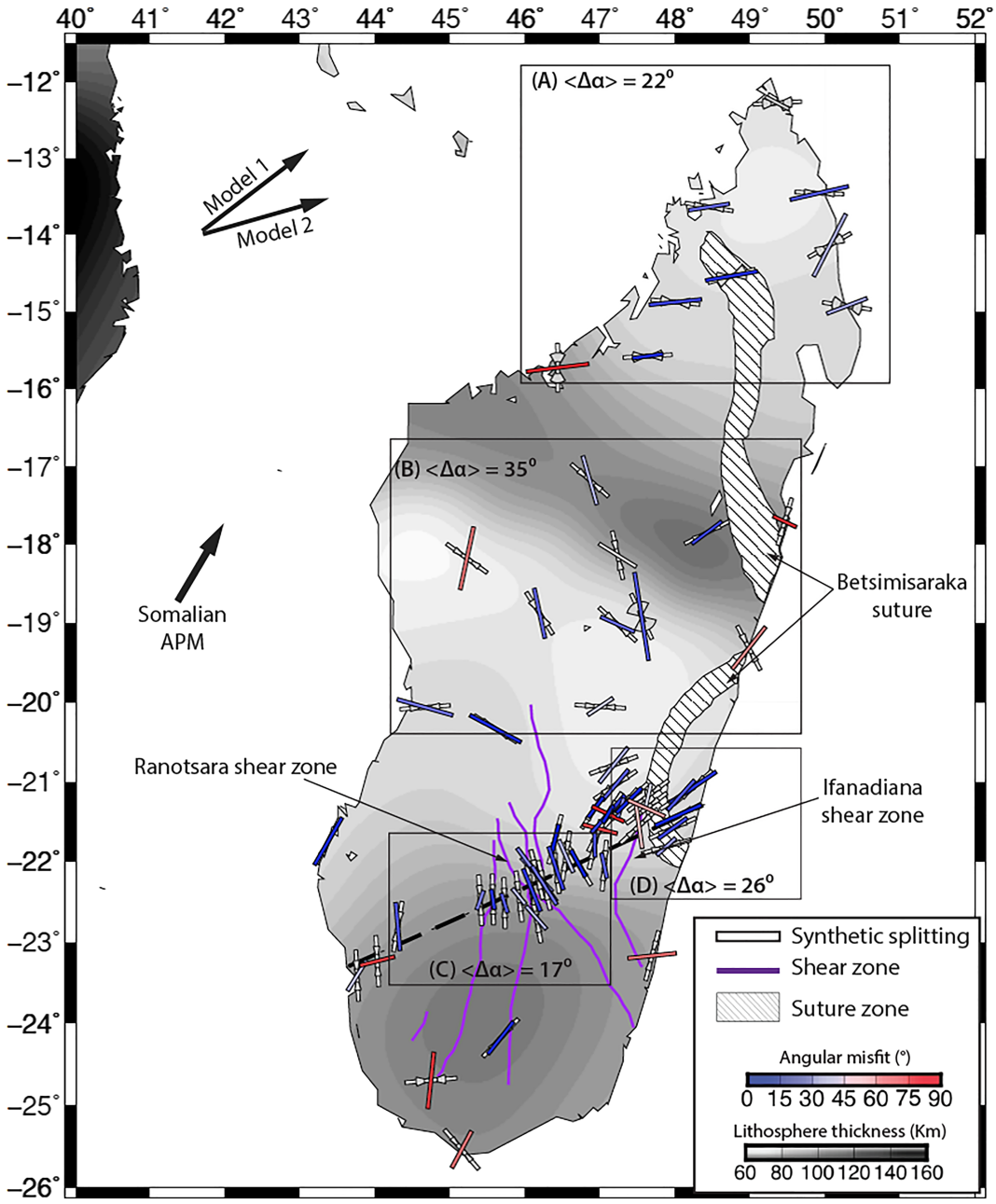

Figure 9. Comparison of synthetic splitting directions derived from EDC model (white bars) with SKS splitting measurement bars colored according to angular misfit (0–90°; Ramirez et al., 2018; Reiss et al., 2016). Gray wedges represent confidence interval associated with the synthetic splitting. Rectangular boxes A, B, C, and D depict key regions and $< \Delta\alpha >$ indicates regional circular mean angular misfit within each rectangular box. Purple lines show shear zones after Martelat et al. (2000). Background gray-scale color shows lithospheric thickness, an updated version of Fishwick (2010). Black dashed line indicates the SELASOMA profile. Black arrows show the Somalian plate APM (Argus et al., 2011), Model 1 and Model 2 are global mantle flow directions from Forte et al. (2010) and Behn et al. (2004), respectively.

4.3. Comparison Between Observed and Synthetic SKS Splitting

In this section, we present the comparison of predicted and observed splitting at individual seismic stations where each of the observations exist (Figure 9). Due to the high variability of the anisotropy orientations in Madagascar, we present the measurements and observations regionally, partitioned into northern, central, south central, and southeast Madagascar, after Ramirez et al. (2018); Table 3. We provide the predicted splitting parameters and TI axes in the PANGAEA repository (doi:10.1594/PANGAEA.909406).

Table 3
A Comparison of the Fit to Anisotropy and Calculated Delay Times for the Three Models Produced in This Work (EDC, Mantle Wind From Behn et al., 2004, Mantle Wind From Forte et al., 2010)

	Observations		Edge-driven convection			Mantle wind from Behn et al., 2004			Mantle wind from Forte et al., 2010		
Region	$<\phi_{obs}>$ (°)	$<\delta t_{obs}>$ (s)	$<\phi_{synt}>$ (°)	$<\Delta\alpha>$ (°)	$<\delta t_{synt}>$ (s)	$<\phi_{synt}>$ (°)	$<\Delta\alpha>$ (°)	$<\delta t_{synt}>$ (s)	$<\phi_{synt}>$ (°)	$<\Delta\alpha>$ (°)	$<\delta t_{synt}>$ (s)
Northern	N68°E	1.00	N85°E	22°	0.92	N65°E	20°	0.78	N47°E	40°	0.89
Central	S39°E	1.00	N60°E	35°	0.88	N55°E	46°	0.71	N57°E	47°	0.92
South central	S20°E	0.66	S18°E	18°	0.76	N31°E	50°	0.67	N23°E	43°	1.02
Southeast	N29°E	0.74	N47°E	26°	0.79	N31°E	37°	0.71	N06°E	32°	0.88

Note. The $<\phi_{obs}>$° and $<\delta t_{obs}>$ are the observed mean fast direction and mean delay time, respectively. The $<\phi_{synt}>$°, $<\Delta\alpha>$°, and $<\delta t_{synt}>$ are the calculated mean fast direction, the mean angular misfit, and the delay time, respectively. The model output files are available at the PANGAEA repository with doi:10.1594/PANGAEA.909406.

4.3.1. Comparison With Edge-Driven Convection-Derived Splitting

For northern Madagascar (Region A; Figure 9), the observed homogeneous fast direction ϕ_{obs} pattern (N63°E) is well reproduced by the EDC model (~N85°E), with a mean regional misfit of 22° (Figure 9). For central Madagascar (Region B; Figure 9) the observed complex fast direction ϕ_{obs} patterns (~S39°E) are poorly reproduced by the EDC model (~N60°E), with a mean regional misfit of 35° . Central Madagascar has 12 SKS splitting observations. The large average misfit is mainly due to two stations at the east and one station at the west. We find a good fit at four individual stations in the center of the region and two stations in the southwest corner with an average misfit less than 15°. For south central Madagascar (Region C in Figure 9) the observed fast direction ϕ_{obs} patterns (~S20°E) are well reproduced by the EDC model (~S18°E), with a mean regional misfit of 18° (Figure 9). LPOs are consistent with the EDC-induced southward flow in south central Madagascar. For southeastern Madagascar (Region D; Figure 9) the observed fast direction ϕ_{obs} patterns (~N029E) are also well reproduced by the EDC (~N47°E) except for two sites that are located on a shear zone. There is a mean regional misfit of 26°.

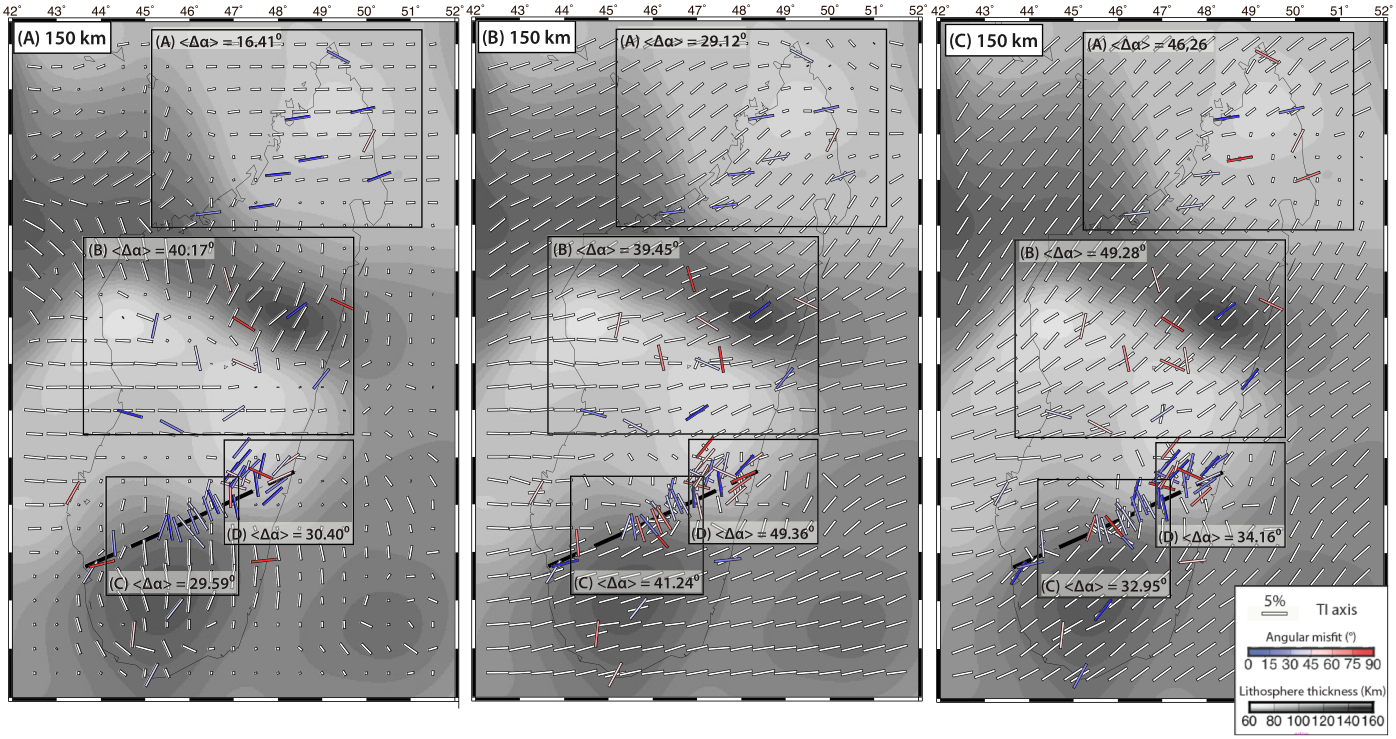

Figure 10. Comparison of calculated TI axes with observations at 150 km depth derived from the: (a) EDC model, (b) mantle wind model for Behn et al. (2004), and (c) mantle wind model for Forte et al. (2010). The SKS splitting measurement bars are colored according to angular misfit [0–90°]. The background shows lithospheric thickness from updated Fishwick (2010). The model output files are available at the PANGAEA repository with doi:10.1594/PANGAEA.909406.

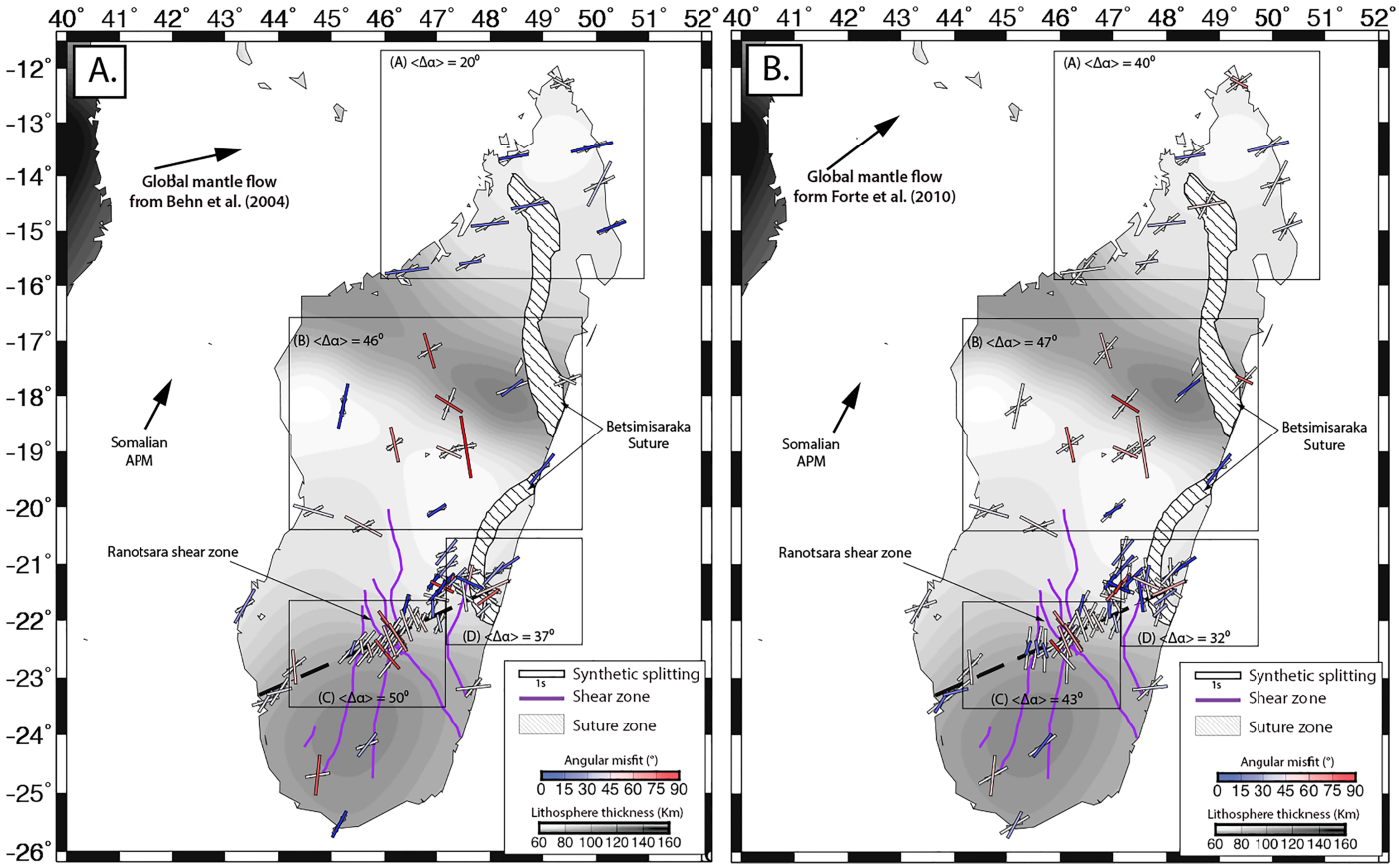

Figure 11. Comparison of synthetic splitting (white bars) derived from lithosphere-mantle wind interactions models with SKS splitting measurement bars colored according to angular misfit (0–90°; Ramirez et al., 2018; Reiss et al., 2016) (a) for Behn et al. (2004) global mantle flow and (b) for (Forte et al., 2010) global mantle flow. Gray wedges represent confidence interval associated with the synthetic splitting. Rectangular boxes A, B, C, and D depict key regions and $< \Delta\alpha >$ indicates regional circular mean angular misfit within each rectangular box. Purple lines show shear zones after Martelat et al. (2000). Background gray-scale color shows lithospheric thickness, an updated version of Fishwick (2010). Black dashed line indicates the SELASOMA profile. Black arrows show the Somalian plate APM (Argus et al., 2011), Model 1 and Model 2 are global mantle flow directions from Forte et al. (2010) and Behn et al. (2004), respectively.

4.3.2. Comparison With Mantle Wind-Derived Splitting

In Figure 10 we show an example of comparison of TI axes with the observations from the three models at 150 km depth and describe below the overall comparisons with calculated synthetic splitting. The TI axis comparisons at different depths are provided in the supporting information. For northern Madagascar (Region A; Figures 11a and 11b), the observed homogeneous fast direction ϕ_{obs} pattern (N63°E) is well reproduced by the Behn et al. (2004) mantle wind model (~N65°E), with a mean regional misfit of 20° (Figure 9), supporting the interpretation that the anisotropy is sourced from below the lithosphere. The Forte et al. (2010) mantle wind model (~N47°E) produces a poor fit, with a mean regional misfit of 40°. For central Madagascar (Region B; Figures 11a and 11b), both Behn et al. (2004) and Forte et al. (2010) mantle wind models produce mean fast azimuth ~S39°E and ~S55°E, respectively, which poorly fit the observed complex pattern ϕ_{obs} pattern (~S39°E) with a mean regional misfit of 46° and 57°, respectively. For south central Madagascar (Region C; Figures 11a and 11b), both Behn et al. (2004) and Forte et al. (2010) mantle wind models produce fast direction patterns (~N31° and ~N23°E, respectively) roughly perpendicular to the observed fast direction ϕ_{obs} patterns (~S20°E) , with a mean regional misfit of 50° and 43°, respectively. Both mantle wind models (Behn et al., 2004 and Forte et al., 2010; ~N31°E and ~N06°E, respectively) in southeastern Madagascar (Region D; Figures 11a and 11b) poorly fit the observed fast direction ϕ_{obs} patterns (~N47°E), with mean regional misfits of 37° and 32° (Figures 11a and 11b). Although several seismic stations in Region D (Figures 11a and 11b) show less than 15° individual angular misfit, the overall calculated patterns show complex fast directions. The complex fast directions are due to patterns of the calculated LPO (TI axis) as well as their variations with depths (Region D in Figures S4 and S5 in the supporting information) from the mantle wind models.

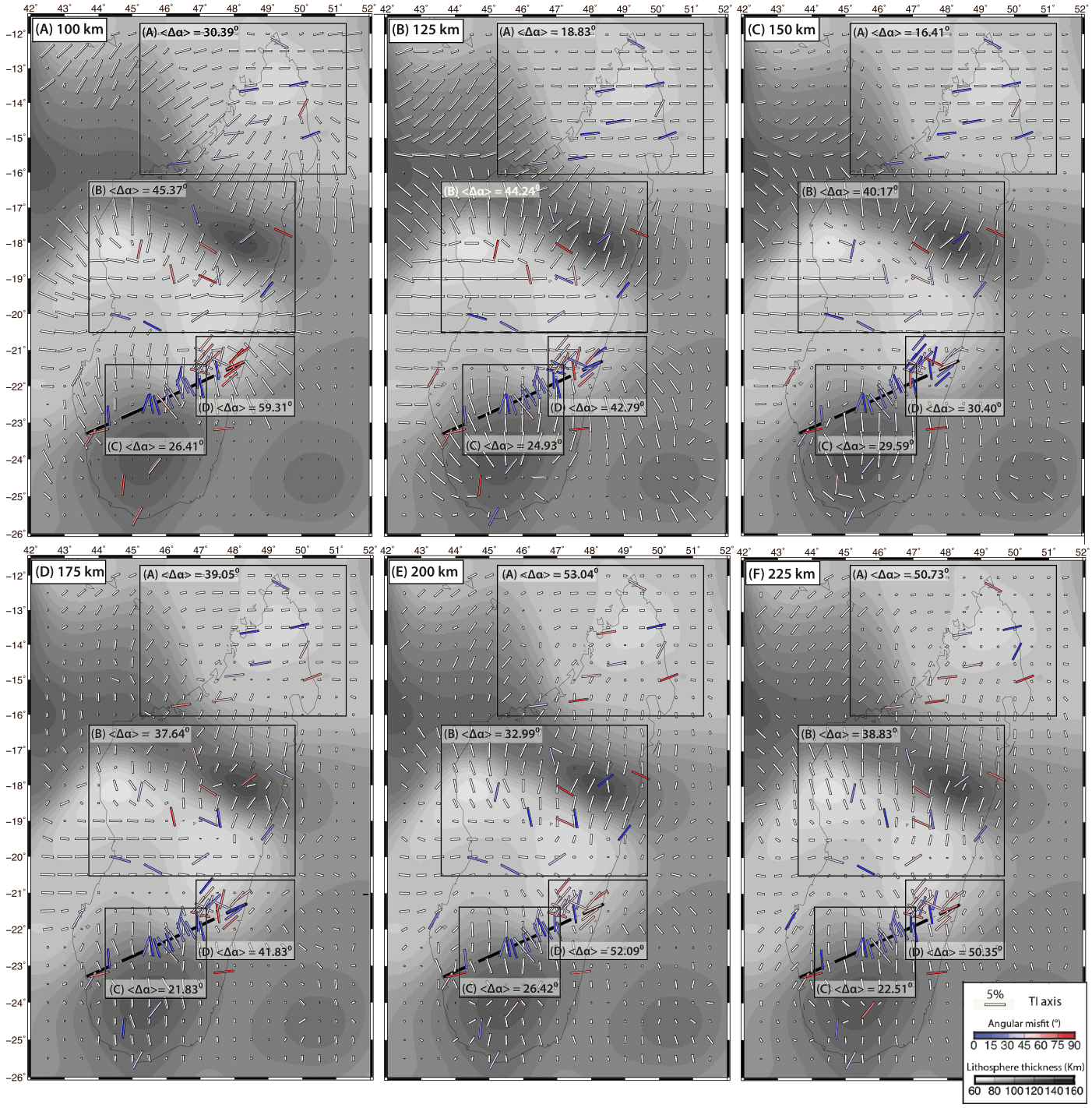

Figure 12. Comparison of TI axes from the EDC model and observed SKS splitting at depth of (a) 100, (b) 125, (c) 150, (d) 175, (e) 200, and (f) 225 km. The SKS splitting measurement bars are colored according to angular misfit [0–90°]. The background shows lithospheric thickness from updated Fishwick (2010). The model output files are available at the PANGAEA repository with doi:10.1594/PANGAEA.909406.

5. Discussion

5.1. Sources of Complex Seismic Anisotropy Beneath Madagascar

Overall, the synthetic splitting fast directions ϕ_{calc}, derived from EDC-induced olivine type-A LPO, are in good agreement with most of the SKS splitting measurements in Madagascar, particularly in the north and the south. In this section, we compare both the predicted splitting orientations and the TI axis orientation

at various depths (Figures 12a–12f) to aid in indicating the depths of the seismic anisotropy measurements since TI can be used as a proxy for LPO.

To determine whether the observed anisotropy in Madagascar can be explained with fossil anisotropy, based on Helffrich (1995), the layer thickness to produce a splitting delay is $L = \frac{dt \times < V_s >}{dV_s}$ where L is the thickness, $< V_S >$ is the average shear wave velocity, and dt is the delay time and dV_S is the percentage anisotropy. Thus, the delay time can be calculated using $dt = \frac{L \times dV_s}{< V_s >}$. Assuming a 4% anisotropy (Savage, 1999) in the lithosphere, an average shear wave velocity of 4.4 km/s (updated from Fishwick, 2010), and an average lithospheric thickness of 80 km for northern Madagascar, the expected delay time that would be due to fossil anisotropy is 0.72 s. For central Madagascar, 0.63 s is the expected delay time for an average lithospheric thickness of 70 km. South central Madagascar exhibits an expected delay time of 0.90 s assuming a 100 km average lithospheric thickness. Finally, the southeastern Madagascar delay time is estimated to be 0.72 s with an average lithospheric thickness of 80 km. The expected delay time due to fossil anisotropy in northern Madagascar and central and southeastern is smaller than the observed average delay time 1, 1, and 0.74 s, respectively. This comparison shows that sublithospheric anisotropy is required to explain the observations in those regions. In contrast, the observed average delay time in south central Madagascar (0.66 s) is lower than the expected delay time due to fossil anisotropy (0.99 s), which indicates that fossil anisotropy contributes to the observations assuming the entire depth extent of the lithosphere in this region has been affected by past orogenic events, which is suggested by Reiss et al. (2016).

5.1.1. Northern Madagascar

The predicted splitting from EDC in northern Madagascar (Region A; Figure 9) aligns well with the observed homogeneous anisotropy pattern (22° misfit) and TI between depths 125 km (Figure 12b; 18° mean misfit) and 150 km (Figure 12c; 16° mean misfit). However, the general patterns of the TI axes do not change dramatically with depth, which is consistent with the small standard deviation of the observations. The tectonic setting of northern Madagascar is characterized by the highly deformed Betsimisaraka suture trending NW-SE (Figures 1 and 9), which trend is inconsistent with the observations, predicted SKS splitting parameters, and TI. The contribution of lithospheric frozen anisotropy can be ruled out since there is only a single station in the center of this region atop the Betsimisaraka suture, and the anisotropic measurement does not align with the feature. In addition, all nine fast directions have delay times larger than 0.5 s (~1 s average) suggesting that the source anisotropy in northern Madagascar is deeper than the crust (Savage, 1999). However, there is a possibility that deep global mantle flow could be a source according to the direction of flow from Behn et al. (2004).

The predicted splitting derived from the mantle wind model align well with the observations for the Behn et al. (2004) global mantle flow (20° misfit, Table 3) and TI between depths 100 km (Figure S4a; 17.01° mean misfit) and Figure S4b; 19.03° mean misfit). However, the predicted splitting does not align for the Forte et al. (2010) global mantle flow (40° misfit, Table 3). This result suggests that the mantle wind model from Behn et al. (2004) slightly improves the fit compared to the EDC-derived splitting alone. The good fit (20° misfit, Table 3) of the observations with the mantle wind from Behn et al. (2004) suggests that the mantle wind from the African Superplume can generate the observed anisotropy in northern Madagascar. This interpretation is consistent with Ramirez et al. (2018).

5.1.2. Central Madagascar

Comparisons of EDC-derived synthetic splitting and observations in central Madagascar (Region B; Figure 9) indicate that the diverging EDC model only partly explains the complex pattern (35° misfit). This region is located in the Antananarivo block, which is cross-cut by the Betsimisaraka suture at the eastern side of the terrain. Only one seismic station lies on the Betsimisaraka suture (Figure 9) and there is a poor fit with the synthetic splitting suggesting there may be a deep source for the anisotropy, which is consistent with the estimated delay times for central Madagascar (0.88 s), or a contribution from fossil anisotropy associated with the Betsimisaraka suture for stations to the east. The comparison with TI is also poor at all depths (minimum regional misfit 33° at 200 km; Figure 12e), which is another indicator the EDC cannot explain all of the seismic anisotropy observations in central Madagascar and consistent with several stations having large standard deviations (>9°).

Our results suggest that the E-W fast splitting in the SW corner of central Madagascar may be due to westward flow associated with the upwelling, radially diverging pattern (Figures 6 and 7). The mismatch (35° misfit) suggests that other effects might have contributed to the anisotropy such as multilayer or tilted-layer anisotropy. Pratt et al. (2017) image a localized low seismic velocity zone beneath central Madagascar that

they hypothesize is a thermal anomaly with a deeper, faster seismic velocity structure to the south that may be from delaminated mantle lithosphere. This feature may locally perturb the EDC, which would produce a pattern that rotates away from the flow pattern calculated in this study. The local perturbation may occur since EDC is considered weak flow that can be easily overwhelmed by local flow driven by temperature anomalies (King & Anderson, 1998).

We also test the potential contribution of mantle wind being deflected around the thick lithosphere as a contributor to the sources of the anisotropy. We find that both models employing Behn et al. (2004) and Forte et al. (2010) boundary conditions do not provide a good fit to the data (46° and 47° average misfits, respectively, Table 3). Due to the high variability in the fast polarization directions in central Madagascar, the anisotropy observations cannot be attributed completely to EDC, global mantle flow, or fossil anisotropy alone. We suggest the anisotropy observations are likely a combination of contributions from the above processes.

5.1.3. Southern Madagascar

The SELASOMA profile shows complex seismic anisotropy measurements (Figures 1 and 9). The measurements are ~N-S in the south central region (Region C; Figure 9) and then rotate to a NE orientation in southeastern Madagascar (Region D; Figure 9). Asthenospheric EDC along the SELASOMA profile is controlled by southward flow that slightly rotates to the southeast, which is induced by a relatively steep lithospheric gradient between central and southern Madagascar (Region C). Our results show that the EDC can explain the sharp variation of azimuthal anisotropy along the SELASOMA profile (Figure 9) with an average misfit of predicted SKS splitting of 18° in south central Madagascar and 26° in southeastern Madagascar (Region D). The comparison with TI axis (Figure 12) shows reasonable agreement with synthetic LPO and observations with an average of 26° in south central Madagascar over all depths, but a less consistent fit to southeastern Madagascar with a minimum misfit of 30°.

Another potential source of the seismic anisotropy in southern Madagascar is fossil anisotropy in the entire lithosphere as suggested by Reiss et al. (2016). In the south central region and part of southeastern region, the geology is characterized by the Ranotsara shear zone that was active during the East African Orogeny ~500 Ma (e.g., de Wit et al., 2001). Reiss et al. (2016) attributed the ~N-S trending azimuthal anisotropy in the south central region, with delay times varying between 0.4 and 1.5 s, to fossilized heterogeneities from this event. However, this interpretation is inconsistent with the rotation of seismic anisotropy along the eastern side of the profile, which suggests an additional source is needed.

In south central Madagascar, the predicted splitting derived from the Behn et al. (2004) and Forte et al. (2010) mantle wind models are poor fits with observations (50° and 43° average misfits, respectively, Table 3). We also find relatively poor fits for both models in southeastern Madagascar (37° and 32° average misfits, respectively, Table 3).

Seismic anisotropy observations in the center of the SELASOMA profile suggest that the observations could result from an integrated anisotropy contribution of two layers or simply from EDC alone. Fossilized lithospheric anisotropy and asthenospheric anisotropy sources could coincidentally align. The relatively large observed delay times can be explained by a contribution from fossil anisotropy in the lithosphere and asthenospheric sources because anisotropy sources confined to the crust can only contribute to a small amount ($\leq$0.3 s) of the measured delay time (see Silver, 1996).

In the eastern part of the profile in the southeastern region (Region D; Figure 9), predicted fast directions from EDC align with an approximately NE orientation consistent with the observations. The alignment suggests that the change in anisotropy direction from the center to the east of the profile is likely due to EDC derived from the decrease of lithospheric thickness to the eastern margin of Madagascar. The relatively large misfit of 26° in the southeastern region (Region D) can be explained by several possibilities. The orientations of the fast directions at three stations in the middle of the region exhibit approximately N-S directions that align with the existing Ifanadiana shear zone (see region D in Figure 9) suggesting a source from preexisting structure. Alternatively, Reiss et al. (2016) suggest that APM induces LPO because the average orientation of the observed anisotropy is parallel to the Somalian plate APM. However, our model suggests that EDC can produce the observations equally well (26°) without accounting for APM or preexisting shear zones, but the abrupt changes in fast direction in the center and west of region D can be better explained with a contribution from the preexisting Ifanadiana Shear Zone.

A recent study by Scholz et al. (2018) supports our interpretations. Scholz et al. (2018) calculate SKS splitting observations mainly in oceanic regions around Madagascar, which is beyond the continental scope of this work, but have two measurements in southern Madagascar. One SKS splitting measurement is ~100 km south of the easternmost terminus of the SELASOMA profile (~S73°E ± 20.4) and the other is approximately 250 km south of the SELASOMA profile on the eastern coast of Madagascar (~N14°E ± 14.5). Since the two measurements on Madagascar are poorly constrained, we choose not to use them in our analysis. Consistent with our interpretation, Scholz et al. (2018) hypothesize that the source of SKS splitting observations on Madagascar may be due to sublithospheric material driven by EDC below a locally thin lithosphere. Scholz et al. (2018) also suggest that most of their anisotropy observations surrounding Madagascar and in the Indian Ocean poorly align with the present-day motion of the Somalian plate. They argue that the Somalian plate motion is too slow, ~2.7 cm/yr (e.g., Argus et al., 2011), such that the shear induced LPOs are expected to be weak (Debayle et al., 2016).

In southernmost Madagascar (Figure 9), two observations appear to align with the existing N-S trending shear zones (Ampanihy and Beraketa, Figure 2). Since only one observation aligns with the EDC-derived splitting (Figure 9) and derived from the mantle wind mode of Forte et al. (2010; Figure 11b), we propose that those observations may be sourced from fossil anisotropy. The observation in the southernmost tip of Madagascar aligns well with the calculated splitting derived from the mantle wind model of Behn et al. (2004). We propose that this observation is sourced from sublithospheric LPO induced by the mantle wind.

5.2. Dominance of Edge-Driven Convection Over Mantle Wind Beneath Madagascar

The overall comparison of calculated splitting shows that EDC model produces a better fit with the observations than the mantle wind models, except in the north where the Behn et (2004) mantle wind model also reproduces the observations. The EDC model can explain the small-scale variations of anisotropy along the SELASOMA profile, but both mantle wind models do not. This result suggests that EDC dominates convective flow in the upper mantle beneath Madagascar, which implies that EDC can develop within the presence of mantle wind. The lithosphere-mantle wind interactions models show that small perturbation (10 mm/yr) from global mantle flow can overwhelm the pattern of EDC to produce mostly horizontal flow. However, several studies suggest that present-day deformation in Madagascar is linked with asthenospheric upwelling (e.g., Paul & Eakin, 2017; Rambolamanana et al., 1997; Rindraharisaona et al., 2013). Therefore, other processes, such as a lithospheric drip, which has been associated with asthenospheric upwelling (West et al., 2009) and potentially imaged beneath central Madagascar (Pratt et al., 2017), may enhance the development of EDC beneath Madagascar. An integrated time-dependent modeling approach that incorporates global mantle flow calculations and edge-driven convection is an area of future research. Based on the results from our approach, we suggest that EDC is critical in explaining the formation of sublithospheric azimuthal anisotropy beneath Madagascar.

5.3. Upper Mantle Rheology Beneath Madagascar

Knowledge of upper mantle rheology is fundamental to the study of mantle dynamics in a region. Rheological properties of sublithospheric continental regions may differ from those of oceanic regions (Karato, 2010). It is commonly accepted that the primary mechanisms for controlling upper mantle deformation are diffusion and dislocation creep with diffusion creep typically dominating sublithospheric mantle (e.g., Karato & Wu, 1993; Nicolas & Christensen, 1987; Ribe & Yu, 1991; Zhang & Karato, 1995). While the diffusion creep mechanism tends to cause random orientations of olivine crystals, and is thus responsible for isotropic aggregates, dislocation creep produces LPO and is responsible for observed seismic anisotropy in the upper mantle (Dziewonski & Anderson, 1981; Karato & Wu, 1993). Determining the depth extent of dislocation creep and diffusion creep deformation has implications for mantle flow patterns, especially for small-scale flow in continental regions. The viscosity of both diffusion and dislocation creep flow laws depends on temperature and pressure. Dislocation creep, or power-law creep, also depends on strain rate (Podolefsky et al., 2004). Thus, the thickness of the dislocation creep layer may depend on the amount of strain rate in the asthenosphere. For example, Podolefsky et al. (2004) found that in oceanic regions, slower plate motion leads to a thinner layer of dislocation creep regime, which produces a thin and weak seismically anisotropic layer. Nevertheless, the depth extent of dislocation creep in continental regions has only been poorly constrained so far.

Here, we examine the depth where deformation changes from dislocation creep to diffusion creep using (1) observed seismic anisotropy and predicted LPO that develop at different depths and (2) the diffusion

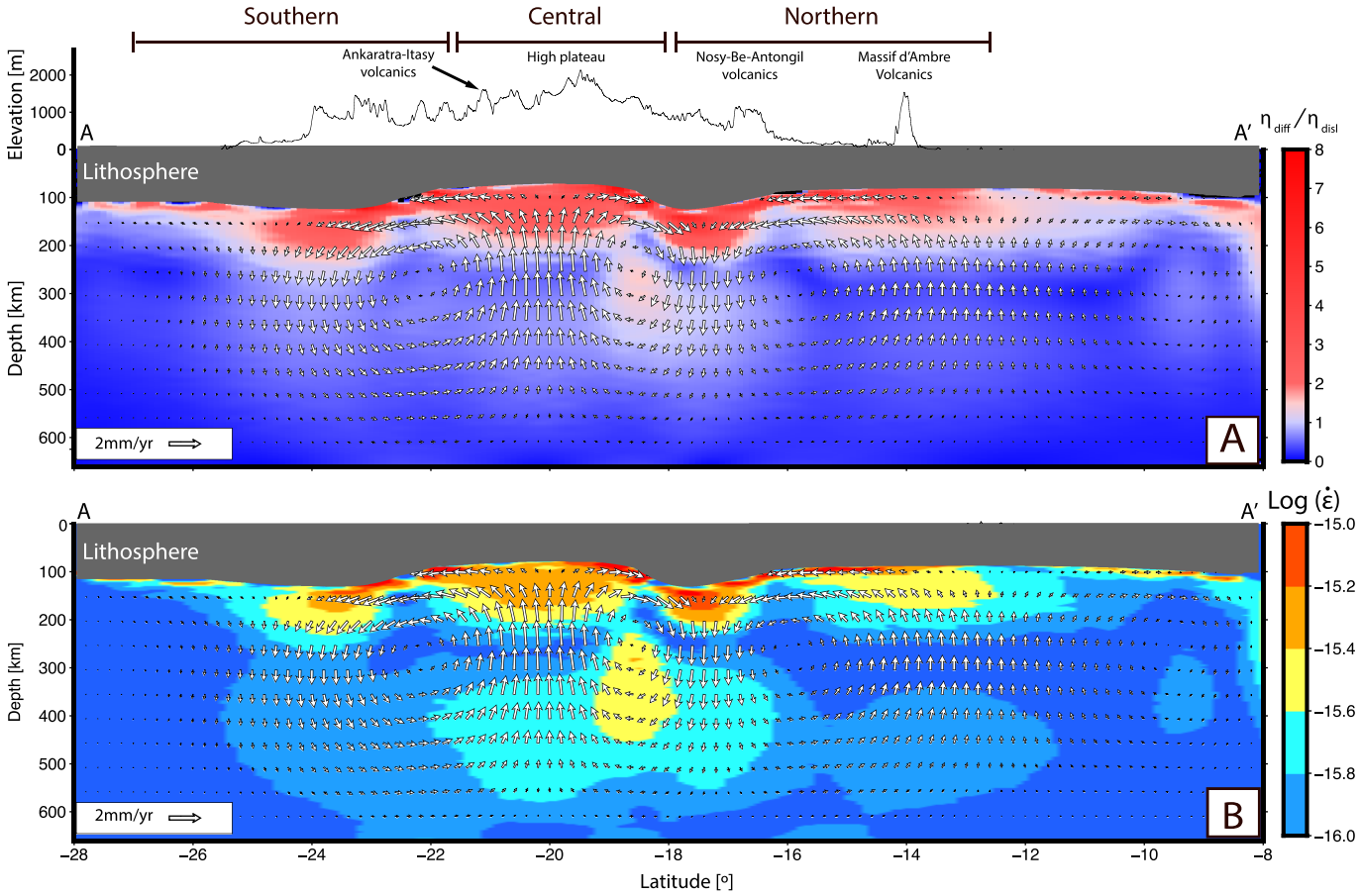

Figure 13. (a) Viscosity ratio (ratio of diffusion creep η_{diff} and dislocation creep viscosity η_{disl}) at the initial model stage across the long axis of Madagascar (profile AA' in Figure 6). Cool colors ($\frac{\eta_{\text{diff}}}{\eta_{\text{disl}}} < 1$) indicate regions dominated by diffusion creep. Conversely, warm colors ($\frac{\eta_{\text{diff}}}{\eta_{\text{disl}}} > 1$) indicate regions where dislocation creep dominates. White vectors represent the asthenospheric flow field. Dry olivine parameters are used for the viscosity calculations, which are obtained from Hirth and Kohlstedt (2003) and are listed in Table 1. (b) Logarithmic scale of strain rate magnitude (square root of the second invariant of the strain rate tensor) across the profile AA'.

creep-dislocation creep ratio (Figure 13a). For northern Madagascar, the good fit between TI axes and observations at 125 and 150 km depth and the decrease in the fit below this depth indicates a change in the rheological regime. Assuming that in that location the LPO results from strain that is accumulated along the upwelling flow beneath northern Madagascar, the asthenosphere undergoes dislocation creep deformation within the 125–150 km channel. LPO beneath this channel might not exist as they could potentially be erased by diffusion creep. There are a few studies that suggest that anisotropy may develop in the diffusion creep regime (Maruyama & Hiraga, 2017; Miyazaki et al., 2013; Wheeler, 2009), but our results indicate shallow sources of anisotropy favoring its formation in the dislocation regime.

Figure 13a shows dominance of dislocation creep in the shallow asthenosphere beneath Madagascar, where strain rate magnitude is relatively large (Figure 13b). The viscosity ratio provides insight into how the EDC controls the thickness of the sublithospheric layer with predominantly dislocation creep regime along the long axis of Madagascar. In central Madagascar, where upwelling is relatively large, the thickness of the dislocation creep regime layer is up to 100 km. A similar thickness of the dislocation creep regime is found beneath the corner of thick to thin lithosphere to the north and to the south of central Madagascar. This dislocation creep channel has similar thickness, but with lower magnitude and decreases rapidly beneath northern Madagascar. The diffusion creep regime dominance is present in the shallow asthenosphere only beneath the oceanic lithosphere in the northernmost and southernmost regions of the profile because of low strain rates in these regions. In zones where diffusion creep dominates beneath oceanic lithosphere, we expect dislocation creep to be limited to the lithospheric mantle.

6. Conclusions

In this study, we employ 3-D geodynamic models of upper mantle flow to investigate the sources of recently observed complex seismic anisotropy patterns in Madagascar and of asthenospheric rheology. Our model workflow involves three steps: (1) modeling of EDC generated by lithospheric thickness variations and modeling lithosphere-mantle wind interactions, (2) calculation of LPO that develops due to these flow calculations, and (3) prediction of splitting shear wave propagating through sublithospheric LPO. Our results show that EDC should be considered as a major source of asthenospheric upwelling beneath Madagascar. Synthetic SKS splitting directions, derived from EDC induced LPO, compare well with most of splitting measurements from Ramirez et al. (2018) and Reiss et al. (2016), except in central Madagascar where EDC may be locally disrupted by an existing thermal anomaly imaged by shear wave tomography. However, we also find mantle wind-derived synthetic splitting from the Behn et al. (2004) model can reproduce observations in northern Madagascar as well.

Our results suggest that EDC contributes to the development of observed anisotropy, and that the role of the Somalian APM and/or global flow is minor, except in northern Madagascar where it may play a role. Upper mantle flow is partly controlled by EDC due to lateral variations of lithospheric thickness. EDC should be considered when interpreting future SKS splitting measurements including measurements across the SELASOMA profile where frozen lithospheric anisotropy exists. Our models indicate that dislocation creep extends up to 200 km into the upper asthenosphere beneath Madagascar, but also that the thickness of the anisotropic layer varies laterally. These results suggest that dislocation creep extends into the asthenosphere beneath some continental regions.

Acknowledgments
This work has been supported by the National Science Foundation (NSF) grant EAR-1551864. Most figures in this paper have been generated with Generic Mapping Tools V5.4.2 (Wessel et al., 2013). We also created one figure with VISIT v2.9 developed by the Lawrence Livermore National Laboratory. The predicted anisotropy model output files are available at the PANGAEA repository with doi:10.1594/PANGAEA.909406. The mantle flow model are available at the Open Science Framework repository with doi:10.17605/OSF.IO/TEJM4. We thank the Computational Infrastructure for Geodynamics for supporting the development of ASPECT, which is funded by National Science Foundation Awards EAR-0949446 and EAR-1550901.

References

Anderson, D. L. (2000). The thermal state of the upper mantle; no role for mantle plumes. *Geophysical Research Letters*, *27*(22), 3623–3626.
Argus, D. F., Gordon, R. G., & DeMets, C. (2011). Geologically current motion of 56 plates relative to the no-net-rotation reference frame. *Geochemistry, Geophysics, Geosystems*, *12*, Q11001. https://doi.org/10.1029/2011GC003751
Austermann, J., Mitrovica, J. X., Huybers, P., & Rovere, A. (2017). Detection of a dynamic topography signal in last interglacial sea-level records. *Science Advances*, *3*(7), e1700457. https://doi.org/10.1126/sciadv.1700457
Ballmer, M. D., Conrad, C. P., Smith, E. I., & Johnsen, R. (2015). Intraplate volcanism at the edges of the Colorado Plateau sustained by a combination of triggered edge-driven convection and shear-driven upwelling. *Geochemistry, Geophysics, Geosystems*, *16*, 366–379. https://doi.org/10.1002/2014GC005641
Bangerth, W., Dannberg, J., Gassmoeller, R., & Heister, T. (2018b). ASPECT v2.1.0 [software], Computational Infrastructure for Geodynamics, Davis, CA. https://doi.org/10.5281/zenodo.1297145
Bangerth, W., Dannberg, J., Gassmöller, R., & Heister, T. (2018a). ASPECT: Advanced solver for problems in Earth's convection, user manual. https://doi.org/10.6084/m9.figshare.4865333
Becker, T. W., Chevrot, S., Schulte-Pelkum, V., & Blackman, D. K. (2006). Statistical properties of seismic anisotropy predicted by upper mantle geodynamic models. *Journal of Geophysical Research*, *111*, B08309. https://doi.org/10.1029/2005JB004095
Becker, T. W., Conrad, C. P., Schaeffer, A. J., & Lebedev, S. (2014). Origin of azimuthal seismic anisotropy in oceanic plates and mantle. *Earth and Planetary Science Letters*, *401*, 236–250.
Becker, T. W., Kellogg, J. B., Ekström, G., & O'Connell, R. J. (2003). Comparison of azimuthal seismic anisotropy from surface waves and finite strain from global mantle-circulation models. *Geophysical Journal International*, *155*(2), 696–714.
Beghein, C., Yuan, K., Schmerr, N., & Xing, Z. (2014). Changes in seismic anisotropy shed light on the nature of the Gutenberg discontinuity. *Science*, *343*(6176), 1237–1240.
Behn, M. D., Conrad, C. P., & Silver, P. G. (2004). Detection of upper mantle flow associated with the African Superplume. *Earth and Planetary Science Letters*, *224*(3-4), 259–274.
Bertil, D., & Regnoult, J. M. (1998). Seismotectonics of Madagascar. *Tectonophysics*, *294*(1), 57–74.
Bredow, E. (2017). Geodynamic models of plume-ridge interaction (Ph.D. Thesis), Universität Potsdam.
Collins, A. (2000). The tectonic evolution of Madagascar: Its place in the East African Orogen. *Gondwana Research*, *4*(3), 549–552.
Collins, A. S., Fitzsimons, I. C., Hulscher, B., & Razakamanana, T. (2003). Structure of the eastern margin of the East African Orogen in central Madagascar. *Precambrian Research*, *123*(2-4), 111–133.
Collins, A. S., & Windley, B. F. (2002). The tectonic evolution of central and northern Madagascar and its place in the final assembly of Gondwana. *The Journal of Geology*, *110*(3), 325–339.
Conrad, C. P., & Behn, M. D. (2010). Constraints on lithosphere net rotation and asthenospheric viscosity from global mantle flow models and seismic anisotropy. *Geochemistry, Geophysics, Geosystems*, *11*, Q05W05. https://doi.org/10.1029/2009GC002970
Corti, G., Cioni, R., Franceschini, Z., Sani, F., Scaillet, S., Molin, P., et al. (2019). Aborted propagation of the ethiopian rift caused by linkage with the kenyan rift. *Nature Communications*, *10*, 1309. https://doi.org/10.1038/s41467-019-09335-2
Dannberg, J., & Gassmöller, R. (2018). Chemical trends in ocean islands explained by plume–slab interaction. *Proceedings of the National Academy of Sciences*, *115*(17), 4351–4356.
de Wit, M. J. (2003). Madagascar: Heads it's a continent, tails it's an island. *Annual Review of Earth and Planetary Sciences*, *31*(1), 213–248.
de Wit, M. J., Bowring, S. A., Ashwal, L. D., Randrianasolo, L. G., Morel, V. P., & Rambeloson, R. A. (2001). Age and tectonic evolution of Neoproterozoic ductile shear zones in southwestern Madagascar, with implications for Gondwana studies. *Tectonics*, *20*(1), 1–45.
Debayle, E., Dubuffet, F., & Durand, S. (2016). An automatically updated *S*-wave model of the upper mantle and the depth extent of azimuthal anisotropy. *Geophysical Research Letters*, *43*, 674–682. https://doi.org/10.1002/2015GL067329
Dziewonski, A. M., & Anderson, D. L. (1981). Preliminary reference earth model. *Physics of the Earth and Planetary Interiors*, *25*(4), 297–356.

Faccenda, M., & Capitanio, F. (2012). Development of mantle seismic anisotropy during subduction-induced 3-D flow. *Geophysical Research Letters*, *39*, L11305. https://doi.org/10.1029/2012GL051988

Faccenda, M., & Capitanio, F. A. (2013). Seismic anisotropy around subduction zones: Insights from three-dimensional modeling of upper mantle deformation and SKS splitting calculations. *Geochemistry, Geophysics, Geosystems*, *14*, 243–262. https://doi.org/10.1002/ggge.20055

Fishwick, S. (2010). Surface wave tomography: imaging of the lithosphere–asthenosphere boundary beneath central and southern Africa? *Lithos*, *120*(1), 63–73.

Forte, A. M., & Mitrovica, J. X. (1996). New inferences of mantle viscosity from joint inversion of long-wavelength mantle convection and post-glacial rebound data. *Geophysical Research Letters*, *23*(10), 1147–1150.

Forte, A. M., Quéré, S., Moucha, R., Simmons, N. A., Grand, S. P., Mitrovica, J. X., & Rowley, D. B. (2010). Joint seismic–geodynamic-mineral physical modelling of African geodynamics: A reconciliation of deep-mantle convection with surface geophysical constraints. *Earth and Planetary Science Letters*, *295*(3-4), 329–341.

Fraters, M., Bangerth, W., Thieulot, C., Glerum, A., & Spakman, W. (2019). Efficient and practical Newton solvers for non-linear Stokes systems in geodynamic problems. *Geophysical Journal International*, *218*(2), 873–894.

Glerum, A., Thieulot, C., Fraters, M., Blom, C., & Spakman, W. (2018). Nonlinear viscoplasticity in ASPECT: Benchmarking and applications to subduction. *Solid Earth*, *9*(2), 267.

Heister, T., Dannberg, J., Gassmöller, R., & Bangerth, W. (2017). High accuracy mantle convection simulation through modern numerical methods. II Realistic models and problems. *Geophysical Journal International*, *210*(2), 833–851. https://doi.org/10.1093/gji/ggx195

Helffrich, G. (1995). Lithospheric deformation inferred from teleseismic shear wave splitting observations in the United Kingdom. *Journal of Geophysical Research*, *100*(B9), 18,195–18,204.

Heron, PJ, Pysklywec, RN, Stephenson, R., & van Hunen, J. (2018). Deformation driven by deep and distant structures: Influence of a mantle lithosphere suture in the Ouachita Orogeny, southeastern United States. *Geology*, *47*, 147–150.

Hirschmann, M. M. (2010). Partial melt in the oceanic low velocity zone. *Physics of the Earth and Planetary Interiors*, *179*(1-2), 60–71.

Hirth, G., & Kohlstedt, D. (2003). Rheology of the upper mantle and the mantle wedge: A view from the experimentalists, *Inside the subduction factory* (pp. 83–105). Washington, D. C: AGU.

Hu, J., Faccenda, M., & Liu, L. (2017). Subduction-controlled mantle flow and seismic anisotropy in South America. *Earth and Planetary Science Letters*, *470*, 13–24.

Jadamec, M. A., & Billen, M. I. (2010). Reconciling surface plate motions with rapid three-dimensional mantle flow around a slab edge. *Nature*, *465*(7296), 338.

Kaislaniemi, L., & van Hunen, J. (2014). Dynamics of lithospheric thinning and mantle melting by edge-driven convection: Application to Moroccan Atlas Mountains. *Geochemistry, Geophysics, Geosystems*, *15*, 3175–3189. https://doi.org/10.1002/2014GC005414

Kaminski, E., & Ribe, N. (2001). A kinematic model for recrystallization and texture development in olivine polycrystals. *Earth and Planetary Science Letters*, *189*(3), 253–267.

Kaminski, E., & Ribe, N. M. (2002). Timescales for the evolution of seismic anisotropy in mantle flow. *Geochemistry, Geophysics, Geosystems*, *3*(8), 1–17. https://doi.org/10.1029/2001GC000222

Kaminski, E., Ribe, N. M., & Browaeys, J. T. (2004). D-Rex, a program for calculation of seismic anisotropy due to crystal lattice preferred orientation in the convective upper mantle. *Geophysical Journal International*, *158*(2), 744–752.

Kaneshima, S., Ando, M., & Kimura, S. (1988). Evidence from shear-wave splitting for the restriction of seismic anisotropy to the upper crust. *Nature*, *335*(6191), 627.

Karato, S. (2010). Rheology of the deep upper mantle and its implications for the preservation of the continental roots: A review. *Tectonophysics*, *481*(1-4), 82–98.

Karato, S., & Wu, P. (1993). Rheology of the upper mantle: A synthesis. *Science*, *260*(5109), 771–778.

Kendall, J.-M. (1994). Teleseismic arrivals at a mid-ocean ridge: Effects of mantle melt and anisotropy. *Geophysical Research Letters*, *21*(4), 301–304.

King, S. D., & Anderson, D. L. (1995). An alternative mechanism of flood basalt formation. *Earth and Planetary Science Letters*, *136*(3-4), 269–279.

King, S. D., & Anderson, D. L. (1998). Edge-driven convection. *Earth and Planetary Science Letters*, *160*(3), 289–296.

Kusky, T. M., Toraman, E., Raharimahefa, T., & Rasoazanamparany, C. (2010). Active tectonics of the Alaotra–Ankay Graben System, Madagascar: Possible extension of Somalian–African diffusive plate boundary? *Gondwana Research*, *18*(2), 274–294.

Langmuir, C. H., Klein, E. M., & Plank, T. (1992). Petrological systematics of mid-ocean ridge basalts: Constraints on melt generation beneath ocean ridges. *Mantle flow and melt generation at mid-ocean ridges*, *71*, 183–280.

Long, M. D., & Becker, T. W. (2010). Mantle dynamics and seismic anisotropy. *Earth and Planetary Science Letters*, *297*(3), 341–354.

Martelat, J.-E., Lardeaux, J.-M., Nicollet, C., & Rakotondrazafy, R. (2000). Strain pattern and late Precambrian deformation history in southern Madagascar. *Precambrian Research*, *102*(1), 1–20.

Maruyama, G., & Hiraga, T. (2017). Grain-to multiple-grain-scale deformation processes during diffusion creep of forsterite+ diopside aggregate: 1. Direct observations. *Journal of Geophysical Research: Solid Earth*, *122*, 5890–5915. https://doi.org/10.1002/2017JB014254

Menke, W., & Levin, V. (2003). The cross-convolution method for interpreting SKS splitting observations, with application to one and two-layer anisotropic earth models. *Geophysical Journal International*, *154*(2), 379–392.

Michon, L. (2016). The volcanism of the Comoros archipelago integrated at a regional scale, *Active volcanoes of the southwest Indian Ocean* pp. 333–344). Verlag: Springer.

Miyazaki, T., Sueyoshi, K., & Hiraga, T. (2013). Olivine crystals align during diffusion creep of Earth's upper mantle. *Nature*, *502*(7471), 321.

Moucha, R., & Forte, A. M. (2011). Changes in African topography driven by mantle convection. *Nature Geoscience*, *4*(10), 707.

Nicolas, A., & Christensen, N. I. (1987). Formation of anisotropy in upper mantle peridotites—A review. In K. Fuchs, & C. Froidevaux (Eds.), *Composition, structure and dynamics of the lithosphere-asthenosphere system* (Vol. 16, pp. 111–123). Washington DC: Am. Geo-phys. Un.

Nicollet, C. (1990). Crustal evolution of the granulites of Madagascar, *Granulites and crustal evolution* (pp. 291–310). Dordrecht: Springer.

Nishizawa, O., & Kanagawa, K. (2010). Seismic velocity anisotropy of phyllosilicate-rich rocks: Characteristics inferred from experimental and crack-model studies of biotite-rich schist. *Geophysical Journal International*, *182*(1), 375–388.

Paul, J. D., & Eakin, C. M. (2017). Mantle upwelling beneath madagascar: Evidence from receiver function analysis and shear wave splitting. *Journal of Seismology*, *21*(4), 825–836.

Podolefsky, N. S., Zhong, S., & McNamara, A. K. (2004). The anisotropic and rheological structure of the oceanic upper mantle from a simple model of plate shear. *Geophysical Journal International*, *158*(1), 287–296.

Pratt, M. J., Wysession, M. E., Aleqabi, G., Wiens, D. A., Nyblade, A. A., Shore, P., et al. (2017). Shear velocity structure of the crust and upper mantle of Madagascar derived from surface wave tomography. *Earth and Planetary Science Letters*, *458*, 405–417.

Raharimahefa, T., & Kusky, T. M. (2006). Structural and remote sensing studies of the southern Betsimisaraka Suture, Madagascar. *Gondwana Research*, *10*(1-2), 186–197.

Raharimahefa, T., & Kusky, T. M. (2009). Structural and remote sensing analysis of the Betsimisaraka Suture in northeastern Madagascar. *Gondwana Research*, *15*(1), 14–27.

Rambolamanana, G., Suhadolc, P., & Panza, G. (1997). Simultaneous inversion of hypocentral parameters and structure velocity of the central region of Madagascar as a premise for the mitigation of seismic hazard in Antananarivo. *Pure and Applied Geophysics*, *149*(4), 707–730.

Ramirez, C., Nyblade, A., Wysession, M. E., Pratt, M., Andriampenomanana, F., & Rakotondraibe, T. (2018). Complex seismic anisotropy in Madagascar revealed by shear wave splitting measurements. *Geophysical Journal International*, *215*(3), 1718–1727.

Ramsay, T., & Pysklywec, R. (2011). Anomalous bathymetry, 3D edge driven convection, and dynamic topography at the western Atlantic passive margin. *Journal of Geodynamics*, *52*(1), 45–56.

Reiss, M., Rümpker, G, Tilmann, F., Yuan, X., Giese, J., & Rindraharisaona, E. (2016). Seismic anisotropy of the lithosphere and asthenosphere beneath southern Madagascar from teleseismic shear wave splitting analysis and waveform modeling. *Journal of Geophysical Research: Solid Earth*, *121*, 6627–6643. https://doi.org/10.1002/2016JB013020

Ribe, N. M. (1992). On the relation between seismic anisotropy and finite strain. *Journal of Geophysical Research*, *97*(B6), 8737–8747.

Ribe, N. M., & Yu, Y. (1991). A theory for plastic deformation and textural evolution of olivine polycrystals. *Journal of Geophysical Research*, *96*(B5), 8325–8335.

Rindraharisaona, E. J., Guidarelli, M., Aoudia, A., & Rambolamanana, G. (2013). Earth structure and instrumental seismicity of Madagascar: Implications on the seismotectonics. *Tectonophysics*, *594*, 165–181.

Rose, I., Buffett, B., & Heister, T. (2017). Stability and accuracy of free surface time integration in viscous flows. *Physics of the Earth and Planetary Interiors*, *262*, 90–100. https://doi.org/10.1016/j.pepi.2016.11.007

Savage, M. (1999). Seismic anisotropy and mantle deformation: what have we learned from shear wave splitting?. *Reviews of Geophysics*, *37*(1), 65–106.

Scholz, J.-R., Barruol, G., Fontaine, F. R., Mazzullo, A., Montagner, J.-P., Stutzmann, E., et al. (2018). SKS splitting in the Western Indian Ocean from land and seafloor seismometers: Plume, plate and ridge signatures. *Earth and Planetary Science Letters*, *498*, 169–184.

Schreurs, G., Giese, J., Berger, A., & Gnos, E. (2010). A new perspective on the significance of the Ranotsara Shear Zone in Madagascar. *International Journal of Earth Sciences*, *99*(8), 1827–1847.

Schuberth, B., Bunge, H.-P., Steinle-Neumann, G., Moder, C., & Oeser, J. (2009). Thermal versus elastic heterogeneity in high-resolution mantle circulation models with pyrolite composition: High plume excess temperatures in the lowermost mantle. *Geochemistry, Geophysics, Geosystems*, *10*, Q01W01. https://doi.org/10.1029/2008GC002235

Seward, D., Grujic, D., & Schreurs, G. (2004). An insight into the breakup of Gondwana: Identifying events through low-temperature thermochronology from the basement rocks of Madagascar. *Tectonics*, *23*, TC3007. https://doi.org/10.1029/2003TC001556

Silver, P. G. (1996). Seismic anisotropy beneath the continents: Probing the depths of geology. *Annual review of Earth and planetary sciences*, *24*(1), 385–432.

Silver, P. G., & Chan, W. W. (1988). Implications for continental structure and evolution from seismic anisotropy. *Nature*, *335*(6185), 34.

Silver, P. G., & Chan, W. W. (1991). Shear wave splitting and subcontinental mantle deformation. *Journal of Geophysical Research*, *96*(B10), 16,429–16,454.

Steinberger, B., Bredow, E., Lebedev, S., Schaeffer, A., & Torsvik, T. H. (2019). Widespread volcanism in the Greenland–North Atlantic region explained by the Iceland plume. *Nature Geoscience*, *12*(1), 61.

Stixrude, L., & Lithgow-Bertelloni, C. (2007). Influence of phase transformations on lateral heterogeneity and dynamics in Earth's mantle. *Earth and Planetary Science Letters*, *263*(1-2), 45–55.

Tian, X., & Santosh, M. (2015). Fossilized lithospheric deformation revealed by teleseismic shear wave splitting in eastern China. *GSA Today*, *25*(2), 4–10.

Tucker, R., Peters, S., Roig, J., Théveniaut, H, & Delor, C. (2012). Notice explicative des cartes géologique et métallogéniques de la république de Madagascar à 1/1,000,000. Ministère des Mines, PGRM, Antananarivo, République de Madagascar.

Wessel, P., Smith, W. H., Scharroo, R., Luis, J., & Wobbe, F. (2013). Generic mapping tools: Improved version released. *Eos, Transactions American Geophysical Union*, *94*(45), 409–410.

West, J. D., Fouch, M. J., Roth, J. B., & Elkins-Tanton, L. T. (2009). Vertical mantle flow associated with a lithospheric drip beneath the great basin. *Nature Geoscience*, *2*(6), 439.

Wheeler, J. (2009). The preservation of seismic anisotropy in the Earth's mantle during diffusion creep. *Geophysical Journal International*, *178*(3), 1723–1732.

Windley, B., Razafiniparany, A., Razakamanana, T., & Ackermand, D. (1994). Tectonic framework of the Precambrian of Madagascar and its Gondwana connections: A review and reappraisal. *Geologische Rundschau*, *83*(3), 642–659.

Zhang, S., & Karato, S. (1995). Lattice preferred orientation of olivine aggregates deformed in simple shear. *Nature*, *375*(6534), 774.

Zhang, S., & O'Neill, C. (2016). The early geodynamic evolution of Mars-type planets. *Icarus*, *265*, 187–208.